UiT
NORGES
ARKTISKE
UNIVERSITET

Faculty of Science and Technology

The impact of Arctic late summer sea ice variability on mid-latitude autumn and winter weather.

—

Patrick Stoll

FYS-3900 Master's thesis in physics 60 SP , November 2015

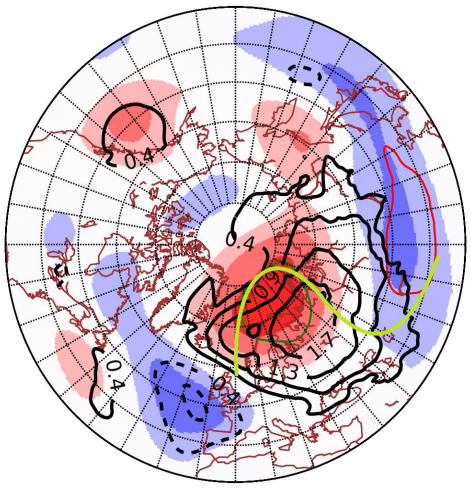

Abstract

The influence of Arctic summer sea ice area on autumn and winter climate in the extra-tropic Northern hemisphere is investigated. During the last decades, the Arctic has warmed more than twice the global average rate, a phenomenon called the Arctic Amplification (AA). AA involves a remarkable decrease of the Arctic sea ice cover and a decrease of the latitudinal temperature gradient. Both are supposed to influence the global energy overturning circulation system, including atmospheric mid-latitude waves and the polar cell.
The present study analyzes how the Arctic September sea ice cover influences the temperature and pressure in the Northern hemisphere extra-tropics in the following months and seeks explanations for this phenomenon in the atmospheric circulation.
To obtain good results, the possible connection of year to year variabilities was studied, and underlying external and internal feedbacks were excluded as much as possible.
Three approaches were taken: Firstly, real world data, such as temperature and surface pressure, expressed by ERA-interim from the year 1979 to 2014, were regressed on the September sea ice area. Secondly, the state of the art climate model CESM with the atmospheric model components CAM4 and CAM5 was used to study and compare the same regressions as in ERA, but for preindustrial conditions. Thirdly, to verify the chain of cause and effect, the consequences of three forced low-ice scenarios of the CESM climate model were compared to a control run.
The first two datasets showed that the Arctic sea ice variabilities are not homogenous throughout the Arctic. Two regions, the Beaufort to East Siberian Sea (Be-ES) region and the Barents-Kara Sea (Ba-Ka) region, with rather independent sea ice area anomaly time series, were observed. Therefore, the climatological response in the two regions was studied independently.

The CESM model runs with forced sea ice conditions give some insight of the winter responses to summer sea ice reduction. In autumn the open water in the Arctic act as heat sources, leading to anomalously warm local temperatures. The local warming leads to extending air and anomalously low surface pressure in the Arctic. This reduces the strength of the polar cell and can lead to a strengthening of the Siberian High in winter.

In ERA-interim and CESM CAM4 & 5 the negative September sea ice anomalies persist into the late autumn for Be-ES and through the whole winter for Ba-Ka.
Autumn responses to the sea ice anomalies are similar between the three datasets for the two regions, while the winter responses contradict each other.
Negative September sea ice anomalies in the Be-ES region seem to induce an East Arctic high pressure in autumn, bringing cold conditions to North Siberia.
Ba-Ka region sea ice anomalies induce a low pressure over its region in autumn, a pattern opposing the one induced by the Be-ES region.
The ERA-interim winter response to the Ba-Ka sea ice anomaly shows an anomalously high pressure over West Russia, bringing cold conditions to Central and East Eurasia. This pattern is refound in literature, but is opposed by the CESM model runs with CAM4 and CAM5.

Contents

1 Introduction

This chapter presents the relevant theory for this thesis and the current state of research on the topic.

1.1 Energy budget

In this chapter, the different Earth's energy fluxes are presented. They can be used to observe changes in the atmospheric energy transport.

Figure 1(a) shows the global annual mean energy budget. The source of energy is the Sun, providing 341 W/m^2 of incoming short-wave radiation of which 102 W/m^2 are reflected. From the net-solar flux 78 W/m^2 are taken up by the atmosphere and 161 W/m^2 by the surface. The surface, idealized as a black

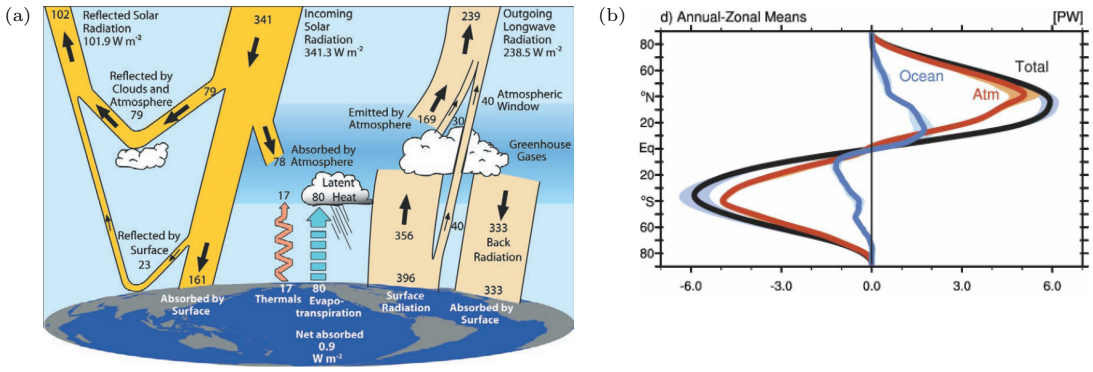

Figure 1: (a) Earth's global annual mean energy budget, from: [Trenberth et al., 2009]. (b) The meridional annual zonal-mean northward energy transport as function of latitude, from: [Fasullo and Trenberth, 2008]. The red line shows the atmospheric, the blue the oceanic and the black the total energy transport. Units are Peta Watt.

body, radiates energy following Stephan-Boltzmann's law. It emits long-wave radiation, in the infra-red part of the spectrum (396 W/m^2). Most of the long-wave radiation is absorbed by so called Greenhouse gases in the atmosphere (356 W/m^2), only some (40 W/m^2) is directly emitted to space, through the so called atmospheric window. The atmosphere radiates a large portion back to the surface (333 W/m^2) and a smaller one out to space (199 W/m^2). The radiation of long-wave radiation by the atmosphere back to Earth is known as the greenhouse effect. It prevents the Earth from strong cooling, especially at night or in winter, times with no or little incoming solar radiation. It is thus responsible for the temperatures being relatively constant in comparison to planets with a thin atmosphere. An increasing amount of greenhouse gases in the atmosphere is, however, leading to increasing global surface temperatures.
Apart from radiation, the atmosphere takes up latent heat (80 W/m^2) and sensible heat (17 W/m^2) from the surface.
Latent heat is released because of evaporation of water at the surface, which condensates in the atmosphere. This phase change releases energy. Sensible heat is the convection of air moving vertically through the atmosphere.

Figure 1(a) depicts global annual mean values of the energy budget. They sum up to zero everywhere if there is no forcing of the climate system. Global warming is denoted in the graphic by a net energy uptake at the surface of 0.9 W/m^2. The annual mean energy uptake of the atmosphere is much smaller because of its smaller mass.

The energy is very close to being balanced in a global annual mean. This is, however, not the case for shorter time scales. There is a net surface energy uptake in spring, which leads to increasing temperatures and a net energy release in autumn.

Furthermore, there are regional differences in the energy balance. The incoming solar radiation decreases with latitude, because the earth is a sphere. Therefore, polar regions are colder than equatorial regions. A spatial energy transport from warmer to colder regions of the world partly compensates this disparity. This mechanism is shown conceptually in Figure 1(b). The atmospheric circulation and the ocean currents transport heat from equatorial regions to higher latitudes. The atmospheric energy convergence is shown in Figure 2. It is responsible for the largest amount of energy transport, especially in the extra-tropical

regions ($>30°$) (see Fig. 1(b)). This is most pronounced in the winters of both hemispheres, when the poleward temperature gradient is highest.

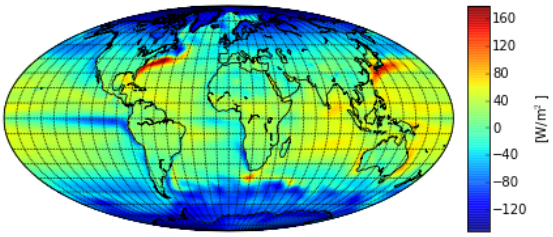

Figure 2: Annual average atmospheric energy budget from ERA-interim (1979-2014). Positive values denote energy uptake of the atmosphere. These are sources of the atmospheric energy flow, also called convergent areas. Negative values denote energy release of the atmosphere, sinks in the atmospheric energy flow, called divergent areas.

The atmospheric energy budget (Fig. 2) is obtained by summing the net short-wave, long-wave, latent and sensible heat fluxes into the atmosphere, coming from the surface and the top of the atmosphere.

1.2 Atmospheric circulation

Chapter 1.1 explains that the meridional difference in solar insolation leads to a poleward temperature gradient and hence to poleward energy transport (Fig. 1). The general atmospheric circulation is presented in Figure 3(a)-(c). It is idealized and shows the first order of the flow.

In the inter tropical convergence zone (red line in Fig. 3(c)), the area with greatest incoming solar radiation, moist air rises, leading to high amounts of precipitation and low pressure at the surface. As the air reaches the upper troposphere, it moves northward in the Northern hemisphere/ southward in the Southern hemisphere. It is deflected to the right/ left by the Coriolis force, forming the subtropical jet stream, in the subtropics (around 30° N/S). This deflection prevents the circulation from reaching higher latitudes. The air descends as dry and warm air to the ground and forms a region of high pressure at the surface of the subtropics. When it moves equator-ward, it is deflected to the right/ left, forming the easterly trade winds. This circulation is called Hadley cell. It is thermally direct, because the circulation transports energy from the equator to the subtropics.

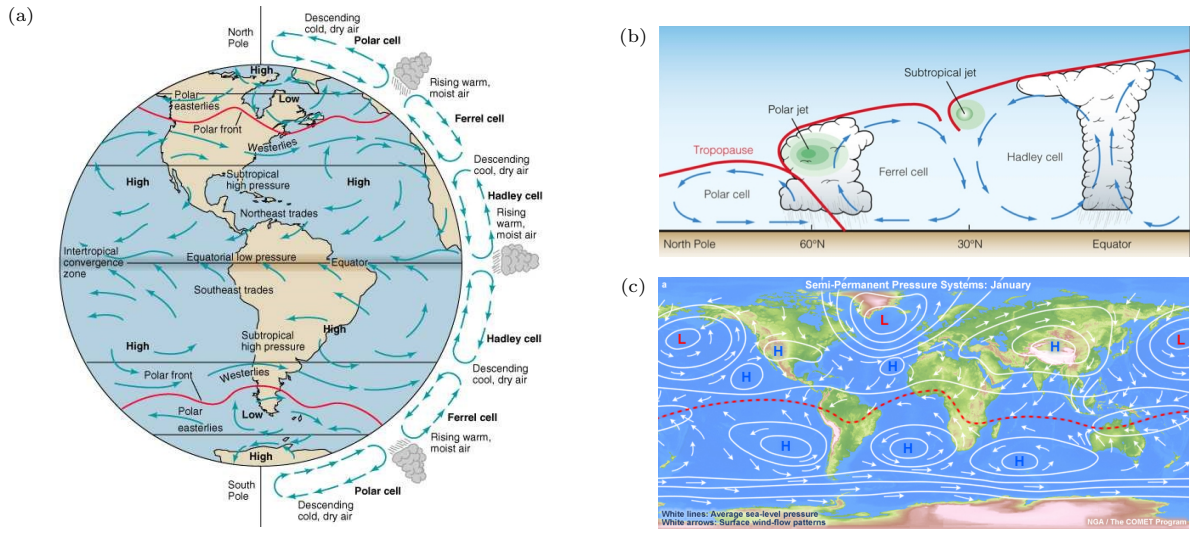

Figure 3: (a) General atmospheric circulation regime [1]. (b) Zonal mean atmospheric circulation [2]. (c) Mean pressure systems and wind vectors at the surface for January [3].

There is a second, much weaker, thermally direct circulation system in the polar regions called the polar

cell. It is driven by cold and therefore dense air, building a high pressure system at the poles, and comparably warm and moist air, creating low pressure systems around the 60° latitude. Air, moving from the polar high to mid-latitudinal lows, is deflected to the right/ left, creating cold polar easterlies.

The mid-latitudinal (30° - 60°) circulation is associated with warm high-pressure systems in the subtropics and cold low pressure systems from around 60°(Fig. 3(a,c)). The dominating wind direction in this area is eastwards. This is explained in the following subchapter.

1.2.1 Geostrophic winds

Geostrophic winds are derived from the horizontal two dimensional momentum equation. It states that the advection is caused by the Coriolis force $\mathbf{F_c} = -\mathbf{f} \times \mathbf{u}$ and the pressure gradient force $\mathbf{F_p} = -\frac{1}{\rho}\nabla_z p$.

$$\frac{D\mathbf{u}}{Dt} + \mathbf{f} \times \mathbf{u} = -\frac{1}{\rho}\nabla_z p \tag{1}$$

where $\mathbf{u} = (u, v)$ is the 2D velocity vector with u being the x = eastward and v the y = northward component. ρ and p are the density and the pressure fields and $\nabla_z = (\frac{\partial}{\partial x}, \frac{\partial}{\partial y})$ is the 2D gradient operator. $\frac{D}{Dt} = \frac{\partial}{\partial t} + \mathbf{u} \cdot \nabla$ denotes the total derivative, where the first term is the local derivative and the second the advection term. $\mathbf{f} = 2\mathbf{\Omega}\sin(\theta)$ is the Coriolis parameter, which depends on the rotation vector of the earth $\mathbf{\Omega}$ and the latitude θ.
Scaling is applied to observe the importance of the terms. Typical atmospheric scalings for length scales and velocities in the mid-latitudes are: $u \sim U = 10\,\mathrm{m/s}$, $x \sim L = 10^6\,\mathrm{m}$. The Coriolis parameter is of magnitude $|\mathbf{f}| \sim f_0 = 10^{-4}\,1/\mathrm{s}$. The time scale is assumed to be advective. This means that the total time derivative of a variable is mainly due to advection. Therefore $1/T = U/L$.
The Rossby number Ro compares the magnitude of the advection term to the Coriolis term of the momentum equation:

$$Ro = \frac{\text{adv. term}}{\text{Cor. term}} = \frac{Du/Dt}{f \times u} = \frac{U/T}{f_0 \cdot U} = \frac{U}{f_0 \cdot L} \tag{2}$$

For the atmospheric values, the Rossby number has a value of order $Ro \sim 0.1$. This means that in the equation of motion, the Coriolis term is an order of magnitude larger than the advection term. Therefore, in first order, the Coriolis force balances the pressure gradient force. This is called the geostrophic approximation. The resulting wind is called geostrophic wind $\mathbf{u_g} = (u_g, v_g)$.

$$u_g = -\frac{1}{\rho f_0}\frac{\partial p}{\partial y}, \qquad v_g = \frac{1}{\rho f_0}\frac{\partial p}{\partial x} \tag{3}$$

This equation shows that the geostrophic wind moves along the isobars or lines of constant pressure. The isobars can therefore be understood as streamlines. The equation shows that, in the Northern hemisphere, the rotation direction is clockwise for high-pressure systems, also called anti-cyclones, and anticlockwise for low-pressure systems, also called cyclones.
It also explains that the dominating wind direction in the mid-latitudes is eastwards. Since the general pressure is dominated by subtropical highs and subpolar lows, there is a negative northward pressure gradient. Using equation 3, this induces eastward winds.

1.2.2 Mid-latitudinal circulation

The circulation in the mid-latitudes is, as above mentioned, driven by a warm subtropical high pressure and cold subpolar low pressure regime. Atmospheric circulation is induced by this imbalance. Although meridional winds are strongly deflected by the Coriolis force, the Hadley circulation is limited by about 30°latitude. In the mid-latitudes atmospheric waves are responsible for the energy transport. They are called Rossby waves if they are of planetary scale, with typically 3 - 6 waves around the hemisphere. For smaller wavelengths, they are called mesoscale waves, and they occur as cyclones.

The mechanism leading to the creation of these waves due to a temperature gradient is described.
The warm and light air in the subtropics and the cold and dense air in the subpolar region lead to tilted geopotential heights through the atmosphere (for a further explanation of geopotential heights, see Chapter 1.2.3). The tilt intensifies with height leading to upper level high pressure in the suptropics and upper level low pressure in the subpolar region. This pressure gradient is created just by the temperature difference, and therefore isobars, lines of constant pressure, isotherms, lines of constant temperature and isopycnals, lines of constant density, are parallel to each other. Such a situation is called barotropic

$p = p(\rho)$ and has the characteristic that the pressure is just a function of density. The state of the atmosphere is shown in Figure 4(a). As described earlier, the isobars can be understood as streamlines.

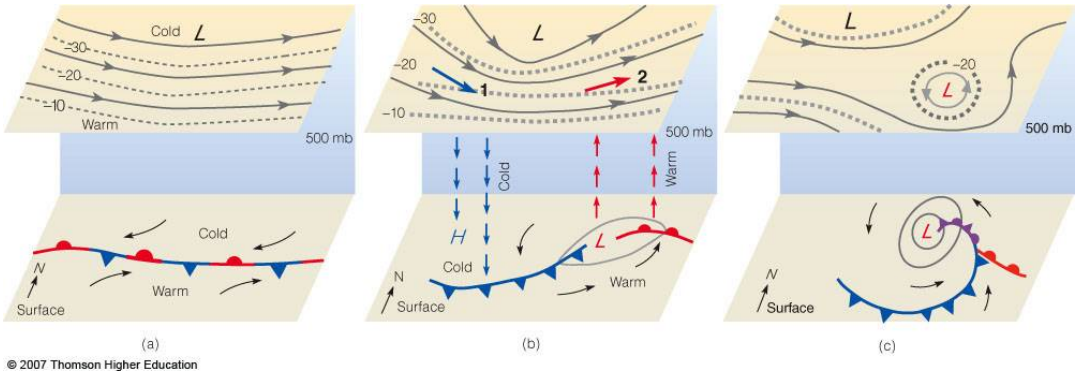

Figure 4: Baroclinic instability [4]. a) shows the initial situation, b) the perturbed state creating instability and c) the formation of a cyclone.

Now, a small pertubation is induced in the form of a low pressure trough in the higher troposphere (see Fig. 4(b)). West of the trough, upper level flow goes across isotherms, bringing air from the cold to the warm region. This is shown by the blue arrow denoted 1. It brings cold and dense air to the region of higher pressure and hereby intensifies the high pressure. It creates a sinking motion, which leads to a surface high west of the upper level trough.
Eastward of the trough, the situation is the opposite. Warm advection into regions of upper level lows intensify the lows pressure systems. The situation, where isobars and isotherms (or isopycnals) cross each other, is called baroclinic, from baro = pressure and clinic = tilt.
The mechanism described here is characterized by a tilt in the pressure with height and therefore called baroclinic instability.
The baroclinic instability leads to cyclones with interacting fronts (see Fig. 4(c)). The meandering of the upper level flow, with such troughs and ridges is depicted in the polar jet stream, which has a strong eastward mean flow. An explanation for the strong eastward winds in the upper troposphere is given in Chapter 1.2.4. The polar jet usually has 3 - 6 waves around the hemispheres. These planetary waves are also called Rossby waves. The propagation of the Rossby waves is dependent on the wavelength and varies from eastward to stationary, to westward. Stationary Rossby waves are responsible for long continuous weather periods. This can lead in extreme situations to long warm/cold periods, droughts and floods.

In an annual and zonal mean, the mid-latitudes also experience a circulation cell, the so called Ferrel cell. In contrast to the Hadley- and polar cell, it is not thermally direct. It is rather caused by the average of the wave induced velocities. The average surface wind direction in the mid latitudes is from subtropics poleward.

1.2.3 Geopotential height

A commonly used variable in geoscience is the geopotential height. It is used to express the vertical pressure in the atmosphere. Differences in geopotential heights display the atmospheric temperature.
The concept is based on the vertical component of the momentum equation. This says that vertical acceleration is due to the gravity force $F_g = -g$ and the vertical pressure gradient force $F_p = -\frac{1}{\rho}\frac{\partial p}{\partial z}$.

$$\frac{Dw}{Dt} = -g - \frac{1}{\rho}\frac{\partial p}{\partial z} \tag{4}$$

where w is the vertical velocity component. A scale analysis of typical magnitudes of the variables shows that the advective term is much smaller than the other terms. Therefore, in the first order, the gravity and the pressure gradient forces balance each other. This is called the hydrostatic approximation:

$$\frac{\partial p}{\partial z} = -\rho g \tag{5}$$

The ideal gas law $p = \rho RT$, which connects the pressure p, density ρ and temperature T with the specific gas constant R, is inserted in the hydrostatic approximation:

$$\mathrm{d}\ln p = \frac{\mathrm{d}p}{p} = -\frac{g}{RT}\mathrm{d}z \tag{6}$$

Integration from the surface $z = 0$ with $p(0) = p_0$ to the level z with $p = p(z)$ gives the barometric formula

$$p(z) = p_0 \cdot \exp\left(-\int_0^z \frac{g}{RT(z)}\mathrm{d}z\right) \approx p_0 \cdot \exp\left(-\frac{gz}{RT}\right) \tag{7}$$

, where in the last step, a constant temperature $T(z) = T$ through the atmosphere is assumed. This is a good first order approximation, although the temperature variations are smaller than the atmospheric mean temperature $\frac{\mathrm{d}T}{T} \ll 1$. The variation of the gravitation is even smaller with height. The barometric formula expresses that the pressure in the atmosphere decreases exponentially with height.
The formula can be inverted to express the height of a pressure value over a reference pressure, which is normally the surface pressure. This is called the geopotential height.

$$z(p) = -\frac{R}{g}\int_{p_0}^{p} T(p)\mathrm{d}\ln(p) \tag{8}$$

Although the temperature variations are small in first order, the geopotential height is fixed for a given pressure value. However, the anomaly of the geopotential height of a given pressure from its mean value is often considered in geosciences. An anomaly can be caused by a difference in the surface pressure p_0 or by differences in the atmospheric temperature $\int_{p_0}^{p} T(p)\mathrm{d}\ln(p)$. The 1000 hPa geopotential height field therefore expresses approximately the same as the surface pressure.

1.2.4 Thermal wind relation

The thermal wind relation shows that the meridional temperature gradient induces a vertical shear in the zonal wind. The mathematical derivation is based on the hydrostatic (5) and the geostrophic wind equation (3). The hydrostatic equation, using the ideal gas law and the definition of geopotential as $\phi = gz$, can be rearranged into:

$$\frac{\partial\phi}{\partial p} = \frac{g\partial z}{\partial p} = -\frac{1}{\rho} = -\frac{RT}{p} \tag{9}$$

which is called the isobaric form of the hydrostatic equation. The x-component of the geostrophic wind equation is rearranged into its isobaric form using the hydrostatic approximation:

$$u_g = -\frac{1}{f_0}\frac{\partial\phi}{\partial y} \tag{10}$$

Taking the vertical derivative in isobaric coordinates of this and inserting the isobaric hydrostatic equation yields the thermal wind relation:

$$\frac{\partial u_g}{\partial p} = -\frac{1}{f_0}\frac{\partial^2\phi}{\partial y\partial p} = \frac{R}{pf_0}\frac{\partial T}{\partial y} \tag{11}$$

The result of this equation is that a meridional temperature gradient induces a sheer in the vertical velocities. Applied on the atmosphere, this means that an equator-ward temperature gradient leads to increasing zonal velocities with height. The zonal velocities reach their maximum around the tropopause, where they form the jet stream.

The phenomenon of the Arctic Amplification (AA), described below, implies a reduction of the north-south temperature gradient. A reduction of the jet-stream due to a smaller temperature gradient has been observed e.g. by [Francis and Vavrus, 2012]. This feature could be explained by the thermal wind relation.
The jet stream influences the mid-latitudinal circulation. A slower polar jet tends to meander more [Francis and Vavrus, 2012]. This can favor the transport of polar air to the mid-latitudes.

1.3 Arctic Oscillation

The Arctic Oscillation (AO) is given as the first Empirical Orthogonal Function of the extra-tropical Northern hemispheric surface pressure field. It describes an often occurring pressure situation.

Empirical Orthogonal Functions (EOF) are an analysis technique to identify patterns of simultaneous variation.
Let $T(x,t)$ be a spatial-temporal field with the spatial dimension M and the temporal dimension N. The time mean is removed to form the anomaly field $T'(x,t)$.
The aim of the EOF analysis is to transform the spatial-temporal field $T(x,t)$ into a spatial pattern of

variability $E^i(x)$, the EOFs, and a temporal projection of these $P^i(t)$, the Principal Component (PC). The anomaly field can be written as a finite sum of EOF fields and its corresponding PC:

$$T'(x,t) = \sum_{i=1}^{M} P^i(t)E^i(x) \tag{12}$$

The aim is to find the EOF which can describe the most variability, and the procedure is as follows:

Σ(x,x) is the corresponding covariance matrix to the anomalous field $T'(x,t)$, calculated by

$$\Sigma(x_k, x_l) = \sum_{i=1}^{N} T'(x_k, t_i)T'(x_l, t_i) \tag{13}$$

Now, the Eigenvalue problem $\Sigma(x,x)E^i(x) = \lambda^i E^i(x)$ where λ^i is the i-th Eigenvalue and $E^i(x)$ the corresponding Eigenvector, is solved. The Eigenvectors are the EOFs. The one belonging to the largest Eigenvalue is the first EOF. The value of the Eigenvalue denotes how much of the variability is described by the corresponding EOF pattern.
The corresponding principle component $P^i(t)$ to the i-th EOF is calculated by the projection of the anomaly field $T'(x,t)$ onto the EOF $E^i(x)$:

$$P^i(t) = \sum_{k=1}^{M} T'(x_k, t)E^i(x_k) \tag{14}$$

In this construction, the PCs are orthogonal to each other, meaning that their correlation is 0. Normally, the first few EOF describe most of the variability, such that the sum in the equation 12 only goes over a few EOFs and PCs. Hereby, the dimension of the data can be decreased enormously. More important is that patterns of simultaneous variability can be identified in the EOFs. These patterns might be connected by the same causes.

The Atlantic Oscillation is defined as the PC to the first EOF of the Northern extra-tropical ($> 20°$ N) hemispheric surface pressure field. The first EOF is shown in Fig 5. In the years 1979 - 2000, it described 19 % of the surface pressure variability.

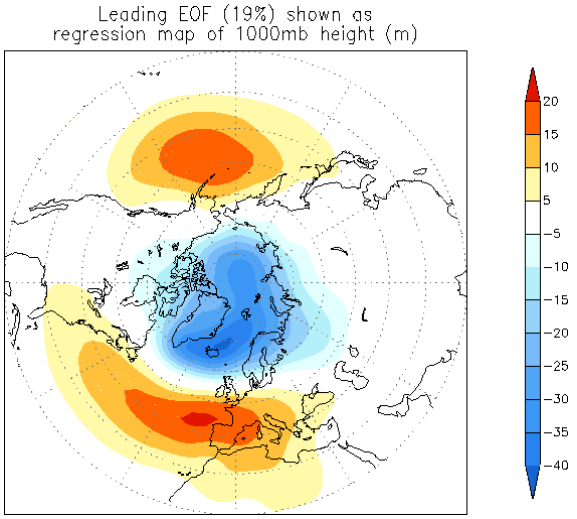

Figure 5: The first Empirical Orthogonal Function (EOF) of the 1000 hPa geopotential height field, based on data of 1979 - 2000. It is connected to a positive index of the Arctic Oscillation [5].

The shown EOF is connected to a positive value of the Atlantic Oscillation (AO+). It is dominated by a polar low pressure, strongest close to Iceland, therefore often referred as Icelandic low, and pronounced high pressure systems over the Azores and the Aleutians.
Due to geostrophic winds, this surface pressure situation leads to a strengthening of the westerly winds in the mid-latitudes, especially in the areas between a high and a low pressure. In winter, it brings warm oceanic air to Eurasia, leading to severe temperatures.
The strengthening of the eastward winds at AO+ situation is also observed in the polar jet stream. It therefore meanders less and keeps cold Arctic air locked in the polar region.
A negative phase of the AO shows opposite features to the positive phase.

1.4 Arctic Amplification and sea ice retreat

The trend of a warming global mean surface temperature has been relatively larger in the Arctic area in the previous decades than the global average, a phenomenon called Arctic Amplification (AA). AA is especially expressed in autumn and winter, while weaker for spring and summer temperatures [Serreze and Barry, 2011].

AA is caused by several mechanisms. The important ones are the sea ice retreat, earlier melting of snow on land, changing horizontal heat flux convergence and increased cloud cover and water vapour.

Figure 6(a) shows the decadal averaged daily Arctic sea ice extent from 1979 to 2012. A significant retreat can be observed for all months within this period. It is most remarkable in summer and early autumn. September sea ice has for example decreased by a rate of 12.4 % per decade [Stroeve et al., 2011], (see also Fig. 8(a)).

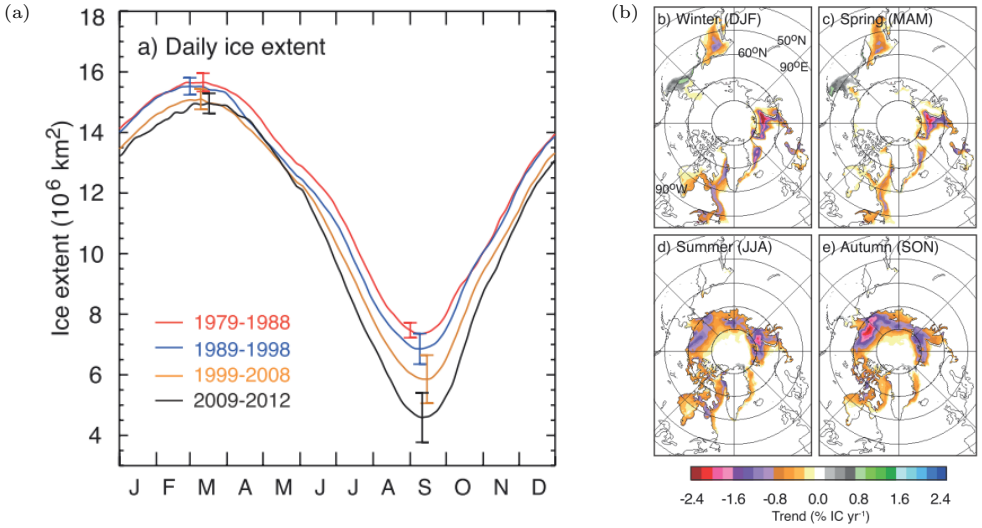

Figure 6: (a) Decadal averages of daily Arctic sea ice extent from 1979 to 2012. (b) Linear sea ice concentration trends from 1979 - 2012 for the four seasons. From: [Vaughan et al., 2013]

Figure 6(b) shows the trend of sea ice change for the different regions of the Arctic. Strongest reductions are observed in summer and autumn for the coastal areas. Especially the Kara Sea in summer and the Chukchi Sea in autumn see large reductions.

This reduced sea ice cover in the Arctic Ocean results in a lower albedo and therefore a higher uptake of short wave solar radiation in spring and summer, which intensifies the melting. The additional energy is mainly stored in the ocean mixed layer (approximately the top 20 m). The effect of summertime ocean heat gain is mainly evident in the following autumn and winter, when the ocean releases sensible and latent heat to the atmosphere. This leads to a later and more slowly freezing icepack. Therefore, spring ice cover is thinner, and the ice will be melted away earlier the following year [Serreze and Barry, 2011]. Graversen et al. [2014], however, argue that the ice albedo effect can only explain about 50 % of the AA.

A warmer atmosphere and more open water in the Arctic leads to a higher amount of water vapor in the atmosphere. Water vapour, being the most important greenhouse gas, increases the down-welling long-wave radiation. An increased cloud cover has a net warming effect in the Arctic, because of polar nights and a low angled sun in spring and autumn, beside for a brief period in Arctic summer. This is in contrast to lower latitudes, where clouds have a net cooling effect [Serreze and Barry, 2011].

Graversen et al. [2008] and Yang et al. [2010] argue that horizontal heat flux convergence in the atmosphere also plays an important role in facilitating AA.
Chylek et al. [2009] shows that Arctic air temperatures are linked to the Atlantic Multi-decadal Oscillation (AMO). The AMO is a multi-decadal mode in the sea surface temperatures in the North Atlantic. They suggest a connection of Arctic warming patterns in 1910 - 1940 and 1970 - today, and the cooling pattern in 1940 - 1970 to the strength of the thermohaline circulation, transporting warm water poleward.

1.5 Impact of the sea ice cover on mid-latitudes weather

Several studies show a coupling between the AA or as reference measurement the Arctic sea ice extend and change in the atmospheric circulation or the regional mid-latitude weather.

Honda et al. [2009] identify a relationship between the Arctic late summer sea ice extend anomalies of a Siberian coast region on wintertime Eurasian climate, based on observational studies and a sensitivity experiment using the atmospheric general circulation model AFES. They conclude that the September sea ice reduction in a Siberian coast region leads to reduced the sea ice cover of the Barents and Kara Seas in late autumn. The reduced sea ice cover in this area induces near-surface diabatic heating, which tends to excite a stationary Rossby wave train in November. The November SLP shows a cyclonic anomaly over the northern part of the Barents Sea and an anticyclonic anomaly extending from Eastern Europe to West Siberia. The upper tropospheric (250 hPa) shift upstreamward by about a quarter wave length relative to the SLP, denoting a baroclinic structure. During the winter the Rossby wave propagates eastward. The mechanism is not fully understood. The surface high pressure anomaly leads to an amplification of the Siberian high and intensifies cold northerlies over the Far East. This gives an explanation for the observed Eurasian winter cold anomalies in years of low September sea ice in the Siberian coast region.

Francis and Vavrus [2012] states that Arctic Amplification leads to a reduced poleward thickness gradient in 1000 - 500 hPa thickness. The reduced geopotential height thickness gradient is, by equation 8, connected to a reduced atmospheric temperature gradient. A reduced poleward temperature gradient is caused by the AA.
The reduced thickness gradient weakens due to the thermal wind relation, the upper level zonal flow. According to Rossby wave theory, it weakens the eastward propagation and increases the trajectory amplitude of the Rossby waves. The amplified flow trajectory is expressed by a northward elongation of 500 hPa ridge peaks in a defined height level.
The slower eastward propagation and the more meandering of the Rossby waves favor slower moving weather systems, which leads to more prolonged weather conditions and thus to more extreme weather.
The connection to the sea ice cover is rather indirect, but lies with the influence of the sea ice cover on the AA.

Screen [2013] observe from forced model runs that Arctic sea ice loss leads to a change in the large scale atmospheric circulation. In summer, it creates a southward shift of the jet stream over Europe. This shift leads to the trend of more precipitation in the Northern European summer. They conclude that the precipitation changes are statistically significant, but small compared to the year-to-year precipitation variability.

1.6 Purpose of the thesis

In the present study, the influence of the late summer Arctic sea ice on the climate of the extra-tropic ($> 30°$N) Northern hemisphere in the following autumn and winter is investigated. The possible influence of the sea ice area change on the atmospheric circulation is evaluated, and consideration are made as to whether this has an effect on the surface temperature.
A scope of the study is also to test different approaches to this question. Thus, three datasets with different qualities that complement each other will be used. Firstly, real world data, expressed by ERA-interim from the year 1979 to 2014, such as temperature, geopotential height (and other parameters) are regressed on the September sea ice area. Secondly, the climate models CESM model with the atmospheric model components CAM4 and CAM5 are used to study and compare the same regressions for pre industrial conditions. Thirdly, to verify the chain of cause and effect, the consequences of three forced low-ice scenarios of the CESM climate model are compared to a control run with climatologically fixed sea ice conditions.
The analysis methods of correlation, regression and composites will be compared to each other and it is discussed that regression expresses the responses to reduced sea ice cover best.

Reflections will also be made on different ways of treating and correcting the different datasets, and choices will be explained before results of the simulations are presented. It is especially discussed whether the ERA-interim dataset should be de-trended linearly or quadratically.
To obtain the influence of the sea ice cover of specific Arctic regions, it the Arctic was split in two areas. The Barents-Kara Sea (Ba-Ka) and the Beaufort-East Siberian Sea (Be-ES) region. The independence of the two areas and the different influence on the atmospheric circulation will be shown.
The atmospheric circulation responds rather differently to sea ice anomalies in the two regions.

A September Ba-Ka sea ice anomaly seems to induce a West Arctic autumn surface low pressure. The winter response varies throughout the different data sets. Some propose the existence of an anomalous Rossby wave or a weakening of the polar cell, leading to anomalously high pressure in Central Eurasia. Others oppose this.
September sea ice anomalies in the Be-ES show autumn surface high pressure anomalies in the East Arctic. This pattern is contrary to the Ba-Ka responses.
Since the responses of the two regions rather oppose each other, the response of the Pan-Arctic sea ice anomaly is diffuse.

Forced modeling studies are used to gain knowledge about the physical processes induced by the sea ice anomaly, and are partly used for comparison to the observations expressed by ERA-interim and free model runs of CESM CAM4 & 5.
The results will be discussed in terms of validity, physical explanation and how they fit into the context of known literature as they are presented.
Conclusions upon the results and suggestions for further work or improvements of the methods will be made.

2 Datasets

To obtain a reliable result, different analysis approaches with several datasets were taken. In this chapter, the origin and treatment of the datasets is presented.

2.1 ERA-interim - observational Experiments

ERA-interim is the recent global atmospheric reanalysis by the European Centre for Medium-Range Weather Forecasts (ECMWF). It covers the period from January 1979 until near-real time. It produces a large variety of parameters in a time resolution from 3- hourly to monthly averages on a spatial resolution of approximately 80 km [Dee et al., 2011].

For this analysis, monthly averaged sea ice cover, surface air temperature, geopotential height, precipitation and energy flux data in a grid of $0.5^\circ \times 0.5^\circ$ for the years 1979 - 2014 was obtained.

De-trending of the data

In the analyses applied to the ERA-data, such as correlations, anomalies from the de-trended climatologies were used. Had the datasets not been de-trended, the correlation between sea ice area (which has a decreasing trend) and the temperature in many areas of the world (which have an increasing trend), would be significantly negative, but the cause of this would mainly be the global warming pattern and thus an external cause affecting both variables. If underlying trends due to external causes are excluded, correlations are more likely to indicate cause and effect. A discussion of the trend correction applied to the data is done in Chapter 4.1.

The sea ice area was here defined as the product of the sea ice concentration and the area of the pixels in the Arctic. It gives the total area covered by sea ice. This is consistent with the definition in the IPCC assessment report 5 [Vaughan et al., 2013]. This differs from the sea ice extent which they define as the area where the ice fraction is higher than 15 %.

Choice of the sea ice month

The aim of these studies is to investigate the late summer/early autumn (ls/ea) effect of sea ice on extratropical Northern hemisphere autumn and winter climate. Therefore a ls/ea sea ice parameter had to be chosen. The quadratically de-trended sea ice anomalies of August and October show a comparable picture to the September anomalies (Fig. 11(c)). The figure does, however, also show that there are differences, which can lead to different results in the data analysis. For example, the years with extremely high and low ice, which exceed one standard deviation, do not match for August, September and October.
In Chapter 4.3, results of the analysis methods based on these three sea ice months are compared. These results are relatively homogeneous. It was chosen to take September, when the sea ice reaches its annual minimum.

2.2 CESM CAM4 and CAM5 - preindustrial conditions

The National Center for Atmospheric Research (NCAR) has developed the Community Earth System Model, version (CESM) to give the scientific community a tool to understand and predict the behavior of the climate [Hurrell et al., 2013]. Here, version 1.2.2 of the model was used. The model system includes component models for the ocean, sea ice, land and the atmosphere. The geophysical fixes across the components are exchanged via a central coupler.
The Community Atmospheric Model version 4 (CAM4) and the latest version 5 (CAM5) were used to make a 100 year coupled simulation with pre-industrial conditions. The first 20 years of these two runs were excluded, to exclude possible shifts of the model run, before coming into a new equilibrium.
CAM5 is an eighth generation atmospheric general circulation model with significant advancement from CAM4. The atmospheric dynamics are treated very similar, but the parameterizations of diabatic processes differ. Especially the treatment of water substances and aerosols was improved [Hurrell et al., 2013]. The parameterization is of CAM4 is more alike to the one in ERA-interim. Therefore both atmospheric model components have advantages in the comparison to ERA-interim.

The monthly averaged output data is in a spatial resolution of $1.9^\circ \times 2.4^\circ$(lat $\times$ lon).

Bandpass filter

Boundary conditions for the pre-industrial model runs are based on data from constant pre-industrial atmospheric composition. With no changing chemical constitution of the atmosphere, no trend of global warming is induced. Because the models are coupled atmospheric oceanic circulation models, they may include long oceanic modes from the slow deep water formation. The ocean overturning circulation shows modes of several years to decades (see Fig. 14(a)). The signal of the influence of the sea ice cover on climate elsewhere is easier to detect if these modes of common underlying causes are excluded. This was therefore done in the present study and documented in Chapter 4.2.

2.2.1 CESM geopotential height problems

The output data from the CESM shows a problem in the geopotential height data. Therefore, responses of the sea ice cannot be shown in higher levels of the atmosphere for CESM model data. This makes physical explanations of the connection between sea ice anomalies and weather responses more difficult.
The problem in the geopotential height fields for CESM is presented here. The 992 hPa geopotential height anomalies (Z_{992}) and the surface air temperatures (SAT), show very similar patterns. This is for example shown in Figure 7(a)&(c) for December of the last year of the model run for CAM5.

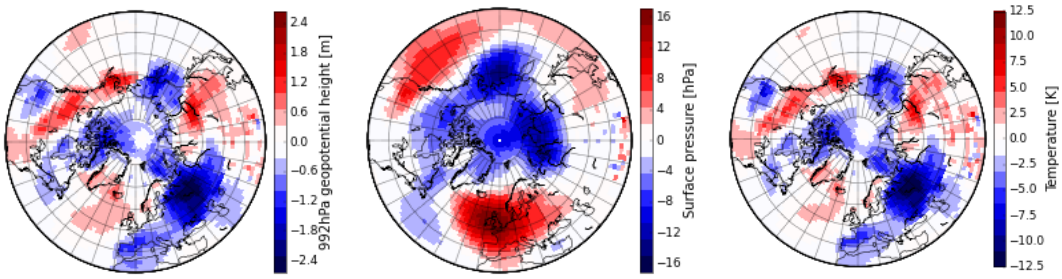

(a) Z_{992} (b) PSL (c) SAT

Figure 7: CESM CAM5 anomalous (a) 992 hPa geopotential height, (b) surface pressure and (c) reference height temperature exemplary for December of the last year of the model run.

This high degree of accordance is unrealistic. One would expect the surface level pressure (PSL) anomalies to be in very high accordance with near surface the geopotential height anomalies, but this is not the case (Figure 7(a)&(b)).
The surface level pressure anomalies can, however, be connected to the temperature anomalies by geostrophic winds. The anomalous anti-cyclone centered over the British Isles brings for example cold winds to East and South Europe, thus responsible for cold anomalies there.
This accordance of the geopotential height with the surface temperature and the disagreement to the surface pressure can be explained in an uncommon way the geopotential height was calculated. For its calculation (equation 8), the reference height p_0 was set to a constant reference pressure instead the surface pressure. In that case the 992 hPa "geopotential height" expresses the mean temperature between the constant referrence pressure and 992 hPa. This is basically the surface pressure.

A correction of the geopotential height field would have been possible, but was not pursued due to time limitations.
Therefore surface level pressures will be used in the following. For the CESM no quantities for higher atmospheric pressures are included in the studies. An inclusion would give further insights in the dependence of the atmospheric circulation to the Arctic sea ice.

2.3 Community Earth System Model - forced model

The CESM is also used for the forced model runs. It is run with a data-ocean mode (DOM), where the sea surface temperatures and the sea ice cover are fixed by boundary conditions.

A control run (CR) was started with pre-industrial sea ice conditions obtained from the Hadley Centre reanalysis. For the analysis of the influence of Arctic sea ice on extra-tropical temperatures, three model scenarios with reduced sea ice conditions were set up. Other boundary data remain the same in the control run and the three constructed scenarios.

Sea ice conditions of the three scenarios

In the **disappear scenario** (DS), the sea ice cover is the same as in the CR for February, the month with maximum ice cover, but vanishes completely in September, the month with minimum sea ice area. The idea is that the SIC difference is large in summer and small in winter, such that the main signal on the autumn and winter weather comes from the summer sea ice reduction.
For the construction, the climatology of the sea ice area of the control run was calculated (blue curve Fig. 8(a)). In the months between the smallest and largest sea ice extend, the sea ice retreat/ recover is amplified in DS (see green curve Fig. 8(a)). The reduced sea ice cover $S_{red}(x, y, t)$ is calculated with the formula:

$$S_{red}(x, y, t) = \frac{\bar{S}(t) - \bar{S}_{Sep}}{\bar{S}_{Feb} - \bar{S}_{Sep}} \cdot S_{Feb}(x, y) \tag{15}$$

where $S(x, y, t)$ is the sea ice fraction at (x, y) at time t of the control run, S_{month} is the sea ice fraction for the given month and $\bar{S}(t)$ is the spatially averaged sea ice fraction for time t.
The sea ice in the disappear scenario vanishes from the maximum extend in February (Fig. 8(b)) with the same fraction in every grid cell. Thus, it is not removed from the boundaries as it does in reality and the control run. Therefore, for some months, areas exist (e.g Hudson Bay in October and November) where

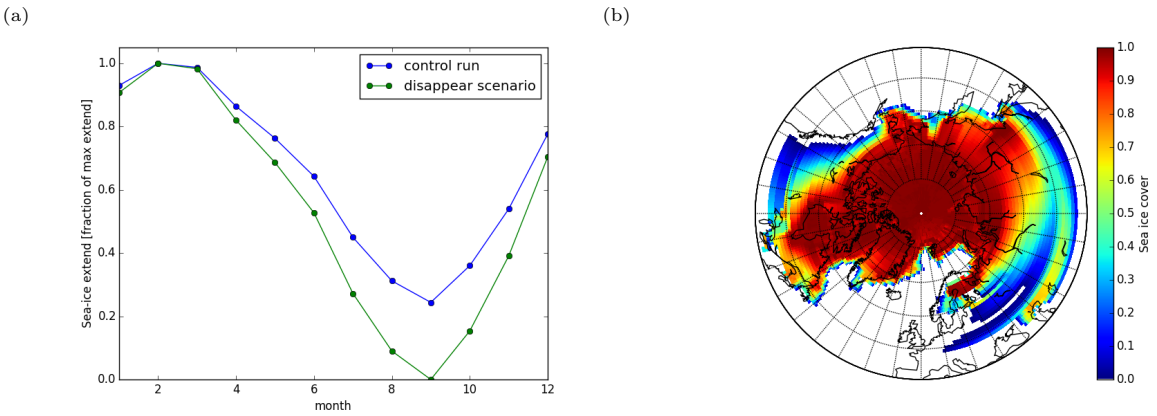

Figure 8: (a) Comparison of the Arctic sea ice area of the control run (blue) with the run where sea ice disappears completely in September (green). (b) February sea ice area of the control run.

the sea ice cover is higher in the disappear scenario than in the control run.
Areas with more sea ice in the disappear scenario than in the control run could have been prevented if the reduction would have been calculated pixelwise:

$$S_{red}(x, y, t) = \frac{S(x, y, t) - S_{min}(x, y)}{S_{max}(x, y) - S_{min}(x, y)} \tag{16}$$

where $S_{min}(x, y)$ is the minimum sea ice cover in pixel (x, y) in the control run. However, not for every pixel the sea ice cover must be in September, especially because there is floating sea ice. The sea ice would therefore not completely disappear in September with this design. This method would also have problems with pixels, where the minimum is equal to the maximum value, such as pixels that have full or no sea ice during the whole year. Therefore, the way of equation 15 is overall easier and was pursued.

The **2012 scenario** (2012S) is a more realistic case of sea ice reduction, lasting the whole year. From this, responses to strong and realistic sea ice anomalies can be studied. For this setup,the sea ice coverage of the year 2012 of ERA-interim was used. 2012 is the year with the smallest summer sea ice cover in the records until now. This scenario has reduced sea ice during the whole year, the tendency being strongest in late summer (August and September).

In the **summer-2012 scenario** (s12S), the sea ice cover is only reduced in summer and in a realistic way. Therefore, the responses to a sea ice retreat only in summer can be analyzed. For the construction, the sea ice coverages of the months July, August and September of the year 2012 of ERA-interim were used, while for the other months, the same conditions as the control run were applied. The input files display the sea ice cover of the middle of the month. The SIC of the intermediate days were interpolated by the model from the middle of the month values. Therefore, the SIC is also reduced in the first half of October compared to the control run, and thus also in the monthly mean of October.

Because of construction discrepancies, the SIC model output of some regions of s12S is different to the CR in winter. The differences are of small magnitude and are considered in Chapter 5.5.

3 Analysis methods

This chapter presents different analysis methods recently used to deal with problems such as the ones in the present study. These are correlations, regressions and composites. At the end, decisions will be made on the most relevant and useful method for the problems at hand.
Correlation does not necessarily imply causality, since the two correlated parameters might have the same underlying factor. In the design of the datasets, known underlying factors, such as globally observed trends, were excluded. A description of this is given in the next chapter. Nevertheless, obtained correlations still only indicate the potential existence of causality. They cannot prove causal relationships.
For simultaneous correlation of two variables, it is unclear, which is the cause for the other, or if both are effects of a third cause. For time-lagged correlations, it is rather the first appearing variable, which causes a change in the second variable. Both can, however, still be caused by a third factor. This disclaimer for correlation relationships must be given for composites and regression methods as well.
To give more evidence to the chain of cause and effect, modeling with induced a forcing is a very useful tool. Although results by the setup model are only explainable by the forcing and not by a third cause.
Three different analysis methods are presented in this chapter. They are, as mentioned above, compared, and arguments for the most proper method to proceed with are made.

3.1 Correlation

The Pearson correlation between two time series was calculated. The Pearson's product-moment coefficient field $\rho(x)_{S,T}$ between the time series $S(t)$ and the field $T(x,t)$ is calculated by:

$$\rho_{S,T}(x) = \frac{\frac{1}{N}\sum_{t=1}^{N} S(t)\cdot T(x,t)}{S_{std}\cdot T(x)_{std}} \tag{17}$$

where $S_{std} = \sqrt{\frac{1}{N}\sum_{t=1}^{N} S(t)^2}$ is the standard deviation of the $S(t)$ and in the same way $T(x)_{std}$ the standard deviation of $T(x,t)$.
The significance of the Pearson's correlation is expressed by the two-tailed p-value. It is calculated from the Monte Carlo approach: By the original dataset $(S(t_i), T(t_i))$, new datasets are created by random permutations of $T(t_i) \rightarrow T(t_j)$. For each of the random and different permutations, the Person's correlation coefficient is calculated. The two tailed p-value is the proportion of the number of permutations, where the magnitude of the correlation exceeds the magnitude of the regarded Pearson's correlation. It shows the probability that uncorrelated variables produce more extreme correlations than the regarded correlation.

Pearson's correlation is based on the assumption that the two time series are both normally distributed. Because this is not necessarily the case, the Spearman rank-order correlation could also be considered. The Spearman correlation is based on monotony between two variables and disregards the magnitude of the values. A high Spearman correlation coefficient between the time series S and T would for example be given if $S_i < S_j < S_k$ and $T_i < T_j < T_k$ independently if S_i is much smaller than S_j and S_k, while T_i is not very different from T_j and T_k.
It was considered better to include the magnitude in the two time series, and to assume a linear relationship. Therefore, the Pearson correlation was chosen.

3.2 Regression

Regression is a method, which expresses the connection of a time series and a field in the unit of the field. In the calculation, it is quite alike correlation. The difference consists of the latter calculating the strength of the connection without displaying the magnitude in units of the fields. Taking into account the magnitude is a property of the regression method. The regression is described in equation (A7) by Wu and Straus [2004].

The regressed field $T_{reg}(x)$ of the field $T(x,t)$ on the time series $S(t)$ is obtained as follows:

$$T_{reg}(x) = \frac{\frac{1}{N}\sum_{t=1}^{N} S(t)\cdot T(x,t)}{S_{std}^2} \tag{18}$$

where $S_{std}^2 = \frac{1}{N}\sum_{t=1}^{N} S(t)^2$ is the variance of $S(t)$.
The regressed field $T_{reg}(x)$ expresses the change in unit of T by a unit change of S. A multiplication by S_{std} gives the change in the regressed field $\hat{T}_{reg}(x)$ as S changes by one standard deviation:

$$\hat{T}_{reg}(x) = \frac{\frac{1}{N}\sum_{t=1}^{N} S(t)\cdot T(x,t)}{S_{std}} \tag{19}$$

This method will be used further in this study, and will referred to as $T(x,t)$ regressed on $S(t)$.

As can be seen from the equations 17 and 19, the difference in the calculation between the Pearson correlation and the regression is that the first is normalized by the standard deviation of the sea ice area and field, while the other is only normalized by standard deviation of the sea ice area. The regression is displayed in the unit of the field variable. It shows the change of the magnitude of this variable as the sea ice area changes by one standard deviation.

For significance calculation of the regression, the Monte Carlo test can be used again. The significance of the Monte Carlo method gives the same results as for the correlation. The reason for this is that the two equations 17 and 19 only differ in the normalization by $T(x)_{std}$. This does not influence the permutation test, because the standard deviation of the temperature variable $T(x,t)$ is constant to permuting years.
The Student's t-test could also be an option for calculation of significance. It has the advantage that it is less computationally intense, because for the Monte Carlo method the regression of several thousand permutations is calculated. The t-test is used to evaluate if the regressed value $\hat{T}_{reg}(x)$ is significantly different from the time mean $\bar{T}(x) = \frac{1}{N}\sum_{t=1}^{N} T(x,t)$ of the field $T(x,t)$. The t-statistic is calculated by:

$$t(x) = \frac{T_{reg}(x) - \bar{T}(x)}{T_{std}(x)/\sqrt{N}} \tag{20}$$

where $T_{std}(x)$ is the standard deviation of $T(x,t)$. The p-value is now calculated directly from the t-distribution.
A strong weakness of the Student's t-test is, however, that it depends on the value of S used for the multiplication in the step from equation 18 to 19. If two standard deviations are taken, as Honda et al. [2009] did, the significance of the results increases a lot. Because of the independence in this factor, the Monte Carlo method was chosen for the present study.

3.3 Composites

Like regression, composites express the connection of a time series and a field in the unit of the field. Composites calculate the mean difference of a field variable $T(x,t)$ for times t, where a regarded time series $S(t)$ fulfills certain criteria. The time series $S(t)$ might be the Arctic sea ice area anomaly. A common criterion is that a value of the anomalous time series exceeds one standard deviation. Years, where the Arctic sea ice area anomaly exceeds or deceeds one standard deviation, are called high ice years and low ice years, respectively (see Fig. 9). The field variables of the high and low ice years are used in the further analyses.

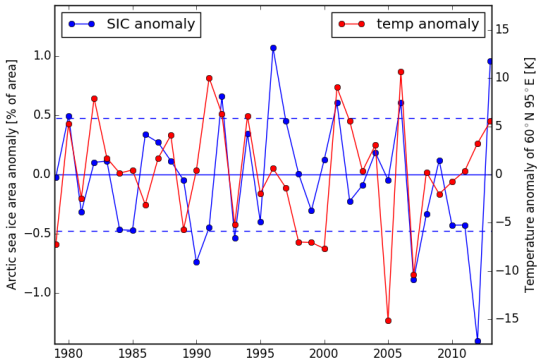

Figure 9: Time series of the years 1979 to 2014 of the quadraticall de-trended Arctic September sea ice area and the temperature of the following January in (60° N, 95° E) High and low ice years are those in which the ice area exceeds one standard deviation from the de-trended climatology (the dotted lines). For the calculation of the composites, the temperatures of the high and low ice years are used. In this example, the negative composites are significantly negative. This means that low sea ice years have low temperatures.

The composite field $T(x)_{comp}$ of the field $T(x,t)$ is calculated by taking the difference between the mean

low ice and mean high ice field variable:

$$T(x)_{comp} = 1/N \sum_{i=1}^{N} T(x,t_i)_{low} - 1/M \sum_{i=1}^{M} T(x,t_i)_{high} \tag{21}$$

where $T(x,t_i)_{low/high}$ is the field of the low ice or high ice year t_i.

The significance of the Composites was calculated by the Student's t-test. It compares field variable distributions of the low ice years T_{low} and the high ice years T_{high} with, possibly, different standard deviations. This procedure is also called the Welch's t-test. The t-statistic was calculated using the following equation ([**?**](6.19)):

$$t = \frac{\bar{T}_{low} - \bar{T}_{high}}{\sqrt{T^2_{std,low}/N_{low} + T^2_{std,high}/N_{high}}} \tag{22}$$

where $\bar{T} = \frac{1}{N}\sum_{i=1}^{N} T(t_i)$ is the mean and $T^2_{std} = \frac{1}{N}\sum_{i=1}^{N}(T(t_i) - \bar{T})^2$ the variance of the ensemble of the low or high ice field variable $T(x,t)$ with N values.
Following the t-distribution, the p-value can now be calculated.

The CESM scenarios with forced sea ice conditions were compared to the control-run of a coupled model. Therefore, the mean of a chosen variable of the control-run was subtracted from the scenario mean. The significance of the difference value was calculated by comparing the two distributions of the chosen variable with the Student's t-test (Equation 22).

3.4 Comparison of the analysis methods

In this subchapter, the three derived analysis methods are applied to the quadratically de-trended ERA-interim data to observe differences in the methods and to argue for a choice of a method in the end.
The time series used is the September Arctic sea ice area anomaly. For this comparison, the field variable is the extra-tropical ($> 30°$ N) Northern hemisphere December temperature anomaly. The following December temperatures are used as responding variable in the anaysis, which makes it a time lag analysis. Later, also other variables such as the surface pressure, the surface energy budget, the sea ice cover and geopotential height will be used as field variables. For easier formulation: It is often not mentioned that the connection of the anomalous fields is analysed.

The outputs from analyses are always portrayed negatively to show the effect of retreating sea ice.
Figure 10 shows the correlation, regression and composites of the September Arctic sea ice area anomaly and the December extra-tropic temperature anomaly.

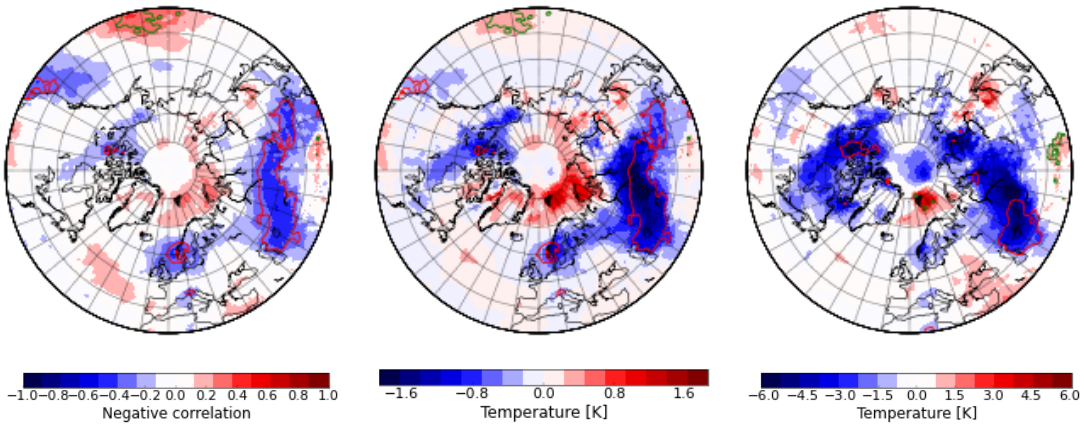

(a) Correlation (b) Regression (c) Composites

Figure 10: (a) Correlation of the quadratically de-trended Arctic September sea ice area anomaly and the December extra-tropical temperature anomaly. The correlation is displaced negatively to show responses for decreasing sea ice. Red/green contours display the 95 % significance level. b) the same for regression and c) the same for composites.

All three fields show same tendencies, but also remarkable differences. The correlation field is unitless and falls between -1 and 1. It is useful to show a connection between the field and the time series, but

it does not give an idea about the magnitude of the field variable. For example, it shows high values in the Pacific Ocean. The regression and the composites show that the magnitude of temperature change was quite small there. This observation is reasonable, since the variation of surface air temperature over the ocean is relatively small, but still has a significant increase in temperature. For the type of analysis, which is the purpose of this study, the magnitude and significance of changes in the variables are both of relevance and important. Since the correlation cannot show the first, correlations will not be used for the present analysis.
As explained above, regressions have the same significance levels as correlations. The field and the significance level of the composites are remarkably different to the regression. Figure 9 shows how the composite is based on 6 high ice and 4 low ice years. The regression is based on the whole 36 years of the time series. Therefore, the statistical basis for the regression is much higher.

Another weakness of the composite method is that it does not take into account by how much the sea ice exceeds over or under one standard deviation. The temperature of a year with reduced sea ice of two standard deviations thus has the same importance as a year with sea ice reduced by only one standard deviation. The magnitude of sea ice variation is taken into account in the calculation of the correlation and regresion.

The regression field has values until 1.8 K, while the composite field has values until 6 K. Both methods calculate responds to different amount of sea ice area change. The composite field is based on temperature values for years with sea ice area difference of more than one standard deviation from the mean. Therefore, the sea ice difference of low ice versus high ice years is in minimum two standard deviations. Figure 9 shows, that for some years the variation in sea ice is of two standard deviations from the mean. Hence, the sea ice difference of low ice versus high ice years is remarkable higher than two standard deviations. With these differences in calculation, it makes sense that the magnitude of the scale is about 3 times bigger for composites than for regressions.

All things considered, regression seems the best and most convenient method to analyze the magnitude of the connection between the sea ice area and other field variables.
For analysis of the connection of two sea ice time series, correlations will also be used in the present study.

4 Development of the analysis setup

In the first two parts of this chapter the preparation of the datasets is presented.
As mentioned, basing analyses on variabilities was considered the best solution. Therefore, the treatment of data was done to exclude underlying causes in the analysis. ERA-interim maintain changes in the atmospheric constitution and therefore global and local trends in climatological variables. CAM4 and CAM5 have a constant atmospheric constitution, but an oceanic mode is observable in their model runs. Therefore underlying causes are treated in different ways for ERA-interim and the coupled CESM model runs CAM4 and CAM5. An argumentation for quadratically detrending is given in the first part of this chapter. The second part presents bandpass filtering for the CAM4 and CAM5 model run.

In the third part argumentation is given to regard sea ice variability responses of September, rather than August, October or November. Responses to these four months are compared.

The last part of this chapter presents, that the Arctic sea ice variability can be described as a linear combination of sea ice variabilities of the Beaufort to East Siberian Sea region and the Barents-Kara Sea region. This makes a separate analysis of the responses to these to regions possible. A separate analysis is useful to recognize effects of the reduced sea ice of that area.

4.1 ERA de-trending

Figure 11(a) shows the Arctic September sea ice area of the years 1979 to 2014 from ERA-interim and its linear and quadratical trend. The linear trend is given by $l(t) = b \cdot t + c$ where b is the linear coefficient and c the offset of the linear trend. The coefficients are derived by least square regression. The uncertainty interval represents a deviation of two standard deviations. This interval represents a 95% significance level.
The linear trend coefficient show that September sea ice area decreased by $b = 615 \pm 152 \cdot 10^3$ km^2 per decade.
More precisely, though, the sea ice area was relatively constant until the late middle of the 90s, but thereafter accelerated its decline until 2014. This is rater represented in a quadratic trend: $q(t) = \tilde{a} \cdot t^2 + \tilde{b} \cdot t + \tilde{c}$, where $\tilde{a}$ and $\tilde{b}$ are the quadratic and linear coefficients and $\tilde{c}$ the offset of the quadratical trend.
The quadratical trend coefficient is showing an increasing retreat sea ice retreat by $\tilde{a} = 252 \pm 141 \cdot 10^3$ km^2 per decade^2. Thus, both leading order trend coefficients are highly significant.

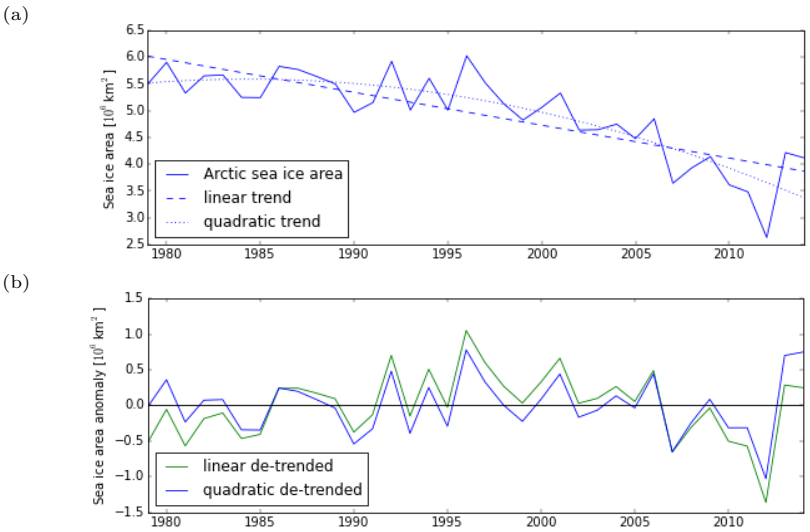

Figure 11: (a) Arctic September sea ice area [10^6 km^2] from 1979 to 2014. The dotted and the pointed lines show the linear and quadratic trend. (b) The linearly (green) and quadratically (blue) de-trended sea ice area anomalies.

The linear and the quadratic trend of the sea ice area anomalies are shown in Fig. 11(b). It is evident that the quadratic trend represents the long-term behavior much better than the linear. The linearly de-trended sea ice area anomalies are negative in the beginning and in the end of the time period, while

they are positive in the middle. The quadratically de-trended anomalies do not show this pattern.

Figure 12 shows the linear (b) and quadratic ($\tilde{a}$) leading order coefficients of the average autumn and winter temperature time series for every grid cell of the extra-tropical Northern hemisphere.

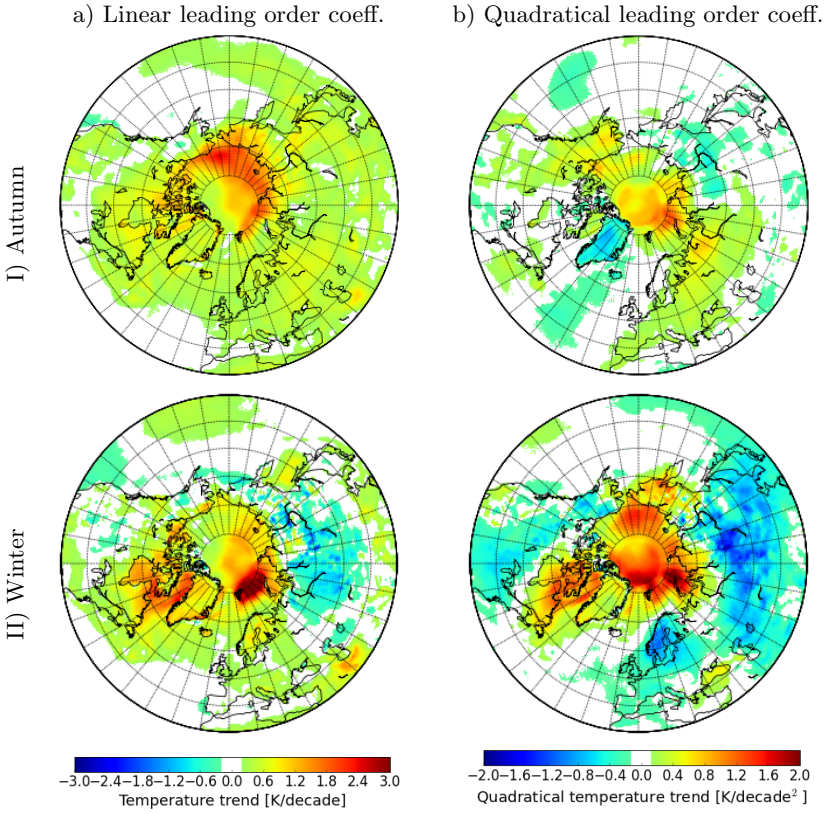

Figure 12: (a) ERA-interim linear and quadratic leading order coefficients of the average autumn (SON) and winter (DJF) temperatures from 1979 - 2014.

The autumn and winter temperature increase is significant (not shown) in most of the Northern hemisphere from 1979 to 2014. This is strongest in the Arctic. Here, the Arctic Amplification becomes visible. Apart from a few smaller regions, only the North west Pacific and Russian winter experienced a cooling trend in this time period.
Figure 13 shows the regressed average winter (DJF) temperatures on the September sea ice area for uncorrected, linearly and quadratically de-trended data. Regression on uncorrected fields was included to compare the de-trending methods to this and to argue for de-trending.
A comparison of the linear trend coefficents of the winter temperatures (Fig. 12(IIa)) and the winter temperatures regressed on the September Arctic sea ice area (Fig. 13(a)) for uncorrected data shows a highly comparable picture between the two, although the scales are different. The September Arctic sea ice area has a strong negative trend. Therefore, the uncorrected regression largely represents the linear trend of every grid cell, while other effects play only a small role.
Regression based on linearly de-trended data (Fig. 13(b)) removes this connection of the linear trends. For example regression on linearly de-trended data disappear for the Hudson Bay and the region south of the Caspian Sea. They show high, positive regressions on untrended data and positive linear temperature trends.
Also new regression patterns appear. Here connected caused by variability played a minor role in comparison to the trends. For example, South Scandinavia, which saw only a small regression when uncorrected, but a positive temperature trend, now has significantly cold temperature regressions for linearly de-trended data.

The conclusion at this point is that although the sea ice area shows a strong linear trend, regression without de-trending mainly shows the local linear trend. The local linear trends are due to large scale causes and locally distinct feedbacks to them. Large scale causes could be global climate change due to

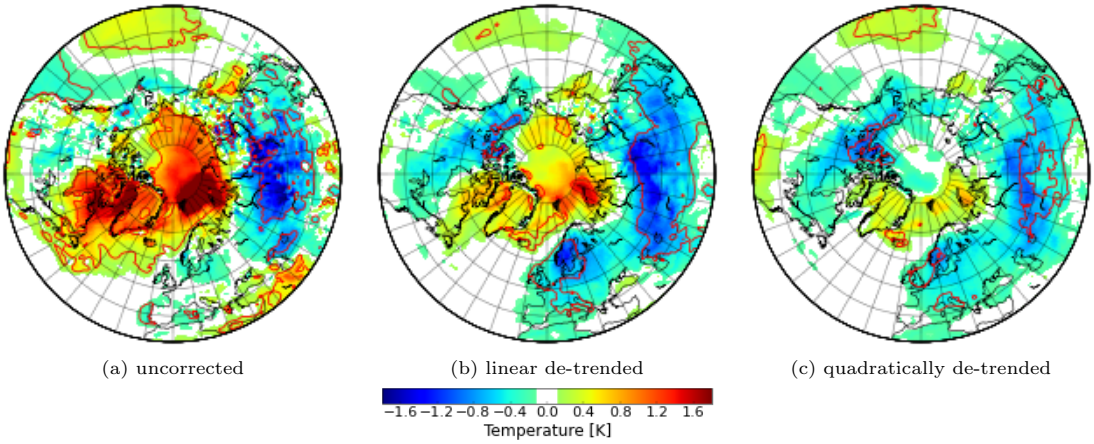

(a) uncorrected (b) linear de-trended (c) quadratically de-trended

Figure 13: ERA-interim average winter (DJF) surface air temperature regressed on Arctic sea ice area of the previous September for (a) uncorrected, (b) linearly de-trended and (c) quadratically de-trended fields. The regression is portrayed negatively. Red contours outline significance level of 90 % and 95 %.

increased greenhouse gas concentration of the atmosphere, or they could be oceanic modes due to long term variations in the thermohaline circulation. It is rather unlikely that the main reason is a linearly decreasing sea ice cover. Therefore, to receive responses from the sea ice cover, the data was corrected for the local linear trends.

In the following the same argumentation is drawn for quadratical de-trending.

The quadratic leading order coefficient in Figure 12(b) shows whether the warming or cooling increased or weakened. In coherence with increasing Arctic sea ice reduction, the warming is also accelerating there. Mid-latitudinal continental regions saw decreased warming in the period from 1979 - 2014.
This is in line with the distinct warming of winter temperatures in the Arctic and mid-latitudinal continents in the periods 1979 - 1997 and 1998 - 2013, which was observed by Kug et al. [2015].

The Arctic thus does not seem to respond linearly to underlying causes. Neither are the temperature changing linearly in mid latitudes. This can be depicted by various regions in the Northern hemisphere observing increasing or decreasing warming trends. Causes may be of large scale or distinct local feedback mechanisms. The first act to influence large regions, possibly including the Arctic in a non linear way. The latter may act to accelerate or restrict local warming. The different regions therefore have different quadratic trends in their climatological parameters.

A comparison of the quadratic trend of the winter temperatures (Fig. 12(IIb)) and the winter temperatures regressed on the September Arctic sea ice area (Fig. 13(a)) for linearly de-trended data shows many similarities between the two. This means that the quadratic trends play an important role in the regression based on linearly de-trended data.

The regression obtained from linearly de-trended data, is vulnerable to being caused by internal causes (local feedbacks) and large scale external effects.
The regression field on quadratically de-trended data (Fig. 13(b)) is based on the year to year variability of the sea ice area and the temperature. It has a smaller amplitude and fewer significant regions than the regression field on linearly de-trended data. The sign of the regression fields are, however, mainly the same.
A quadratic de-trending was therefore considered best for the analysis of sea ice influences on the Northern hemisphere extra-tropical climate, so as to exclude as many external effects as possible. This was done for every month and every grid-cell independently, because the effect of the underlying trends have different magnitudes for the months (see Fig. 6(a)). The focus of the analyses is thus how the year to year variability of the quadratically de-trended Arctic sea ice area, influences year to year climate.

A disclaimer needs to be added, though. It is possible that the quadratic trends are also partly connected to each other by cause and effect, and if that is the case, the signal will be diminished by this choice of

correction.

No evidence was found in literature of studies in a related subject, where quadratic de-trending on observational data was applied. Most commonly, data is linearly trend corrected. This might affect the comparison of results to other groups. Honda et al. [2009], for example, de-trended the sea ice concentration linearly. For their purpose, a linearly de-trended sea ice concentration might be sufficient, because they investigated the period 1979 - 2007 of a chosen area (the Siberian coast). Until 2007, the acceleration of sea ice reduction was not as remarkable as in the following years, so that a linear de-trending was sufficient. The acceleration, which makes a quadratic de-trending preferable, might also not occur in all Arctic regions, and for some regions, linear de-trending might therefore be sufficient.

4.2 CESM CAM4/5 bandpass filtering

The CESM coupled model runs with the atmospheric components CAM4 and CAM5 including an oceanic model and therefore also oceanic modes.
To study the influence of the SIC variability to other climatological variables, the connection of the year to year variabilities is analyzed and underlying causes are excluded as much as possible.

Regressions for CAM4 between the September Arctic sea ice area anomaly and surface temperatures anomalies in the following months show patterns of high amplitude in the Arctic and Pacific ocean. This is for example shown in Figure 14(b) for the September temperatures regressed on the September Arctic sea ice area.

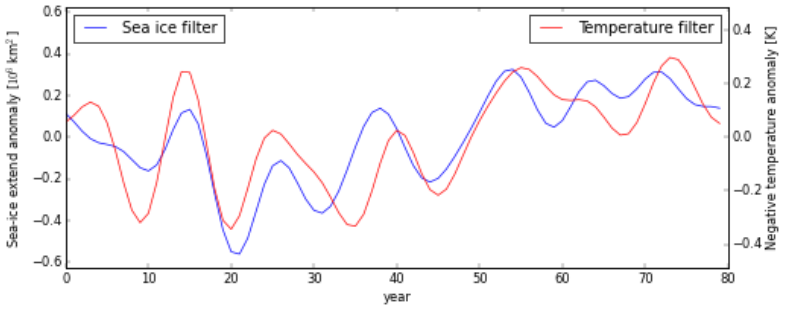

(a) Modes > 4 years

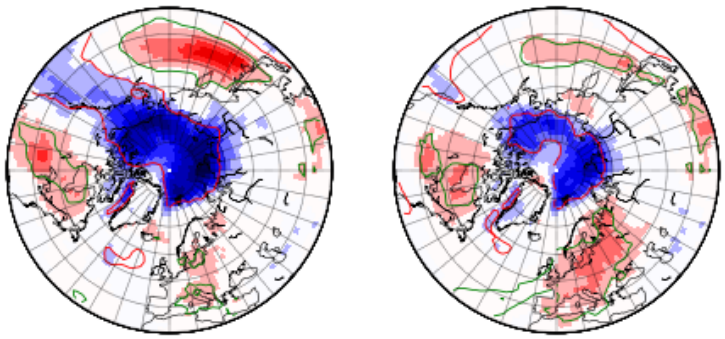

(b) Without filter (c) Filter $n = 4$ years

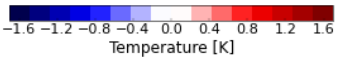

Figure 14: a) CESM CAM4 September sea ice and average extra-tropical Northern hemisphere temperature times series of the modes > 4 years. These are excluded by the bandpass filter. b) September SAT regressed on the September Arctic sea ice area anomalies without filter correction. The regression is portrayed negatively to show responses to reduced sea ice conditions. Red/green lines show the 95 % confidence interval by permutation testing. c) The same for filter corrected data with a filter period of $n = 4$ years.

To avoid this disturbance of the analysis, a Bandpass filter was applied to all data of the CESM coupled model runs: The Fourier transformation was applied to the time series including all months of the model

run. Modes longer than n years, the filter period, were excluded and the time series was inverse Fourier transformed. The time series of modes longer than $n = 4$ years of the September Arctic sea ice area and the mean Northern hemisphere extra tropical September surface temperature are shown in Figure 14(a). These are the modes that were excluded for the analysis. The two time series show a very high correlation to each other, because the oceanic modes influence both the Arctic sea ice and the temperature in the Northern hemisphere.
This pattern of common underlying causes is excluded with the Fourier filter correction. Figure 14(c) shows the same regression as Fig. 14(b), but for corrected data. The filter was applied to every grid cell independently. The strong temperature field in the Pacific and Arctic Ocean was thus reduced.

Different filter periods n were compared. This led to the conclusion that filters with a high filter period ($n \gg 4$) do not exclude correlations by oceanic modes sufficiently enough, because the oceanic patterns, while filters with a small filter period ($n \ll 4$) decrease the year to year variability of the data. A good compromise between the two extremes was a filter period of $n = 4$ years

4.3 Regression on different months

In this subchapter, the results of the regressions based on the Arctic sea ice area of August, September, October and November are compared to investigate if there are remarkable differences between the months. Figure 15 shows the three time series of the quadratically de-trended sea ice areas of August, September and October.

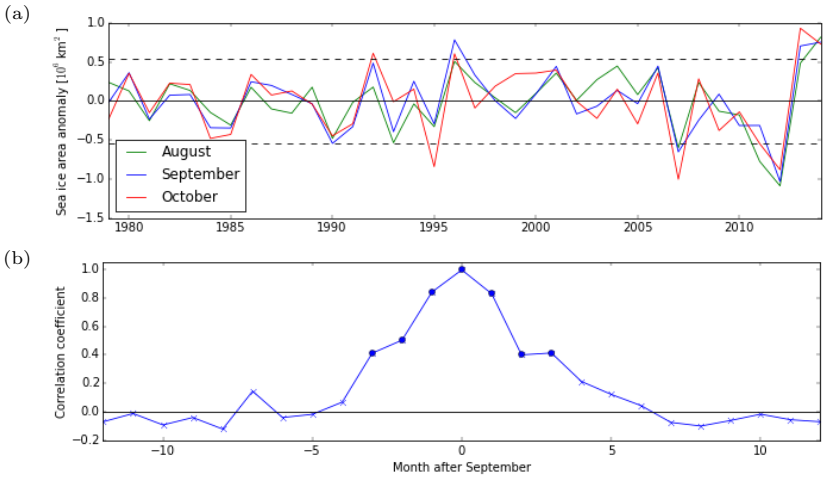

Figure 15: (a) ERA-interim quadratically de-trended sea ice area anomalies of August, September and October. The dashed line denotes one standard deviation of the September sea ice anomalies. (b) Lead-lag-correlation of the monthly averaged Arctic sea ice area with the September sea ice area. Blue dots mark values with a significance higher than 0.95 by permutation testing.

The sea ice area anomalies of August, September and October are highly correlated, because the melting and freezing of sea is a relatively slow process. Therefore anomalously low sea ice cover in one month is responsible for lower sea ice cover in the following month.
Figure 15(b) shows the Pearson correlation coefficients of the sea ice area of September with the preceding and following months. The Pearson correlation coefficients between August and September (0.84), between September and October (0.83) and between August and October (0.77) are highly significant. The memory of the September sea ice area is still significant, but much weaker in November and December, and vanishes thereafter. The same can be seen for the lead correlation. June, July and August sea ice retreat determine the September status, while the months before are of little relevance.

In Figure 16 the average winter (DJF) sea ice cover (a), 850 hPa geopotential height (b) and temperatures (c) are regressed on the August (I), September (II), October (III) and November (IV) sea ice area.
A short time lag is given for regression of winter fields on November sea ice, while a longer time lag for regression on August and September sea ice. For a shorter time lag, the connection of the sea ice area is relatively direct to the variable of the regressed field. However, the direction of causality is unclear. Also, common underlying causes, such as circulation patterns, influence both the sea ice and the

regressed field variable. The atmospheric circulation patterns are normally not persistent over several months, and therefore their influence is strongest for short time lags. Hence, regressions with short time lags are more likely to presenting a connected state of the climate and it is difficult to draw a chain of causality. For longer time lags it is rather the first variable causing the other and typical atmospheric circulation patterns causing a change in the first variable are likely not persisting over the long time period.

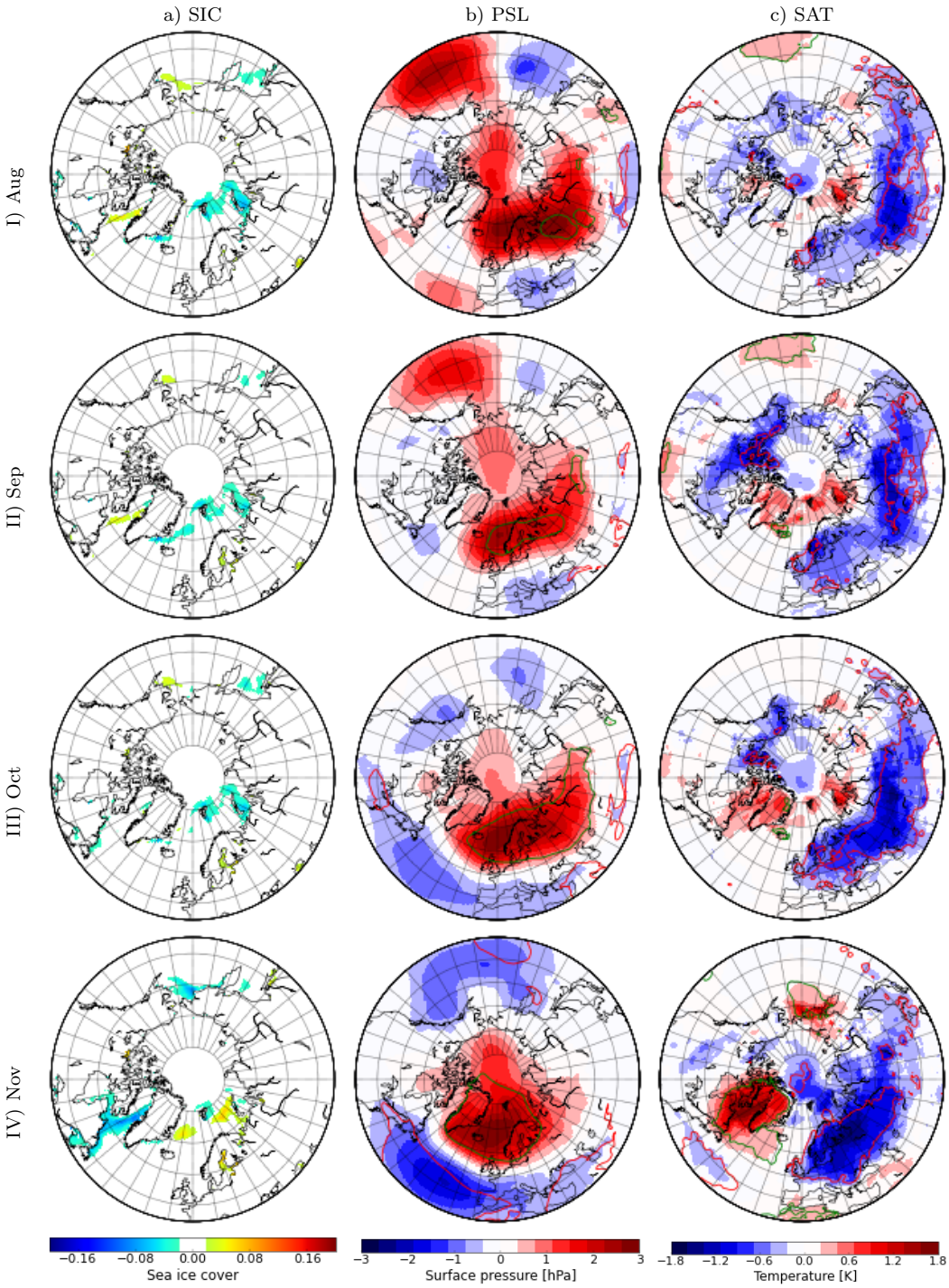

Figure 16: ERA-interim average winter (DJF) (a) sea ice cover (SIC), (b) surface level pressure (PSL) and (c) surface air temperature (SAT) regressed on Arctic sea ice area of the previous (I) August, (II) September (III) October and (IV) November. The regression is portrayed negatively. Red contours outline significance level of 90 % and 95 %.

In the following the data presented in Figure 16 is used to support this argumentation.

The winter mean sea ice memory from the August and September sea ice area, respectively, is very similar for the two months (Fig. 16(Ia) & (IIa)). While the response of the winter sea ice on the November sea ice area (IVa) is very different. An comparison of the September and November fields representing one standard deviation of SIC (not shown), reveals that the November sea ice anomaly is only partly caused by the late summer sea ice anomaly.
Now the situation related to the November sea ice area anomaly is analyzed in more detail, to argue that the November sea ice anomaly and its winter responses are both connected to the Arctic Oscillation.

The negative mode of the Arctic Oscillation (AO) is an obvious feature in the regressed winter surface pressure field on November sea ice (IVb). The positive mode of the AO is shown in Figure 5.

The November sea ice area and the AO probably have the same underlying causes which may be as following: The conditioning pressure fields of October and November observe significant high pressure anomalies over the Arctic (not shown). This strengthen the polar cell and increase the energy flux to the Arctic, leading to slower autumn sea ice return.
October and November Arctic high pressure also favors high pressure conditions during the winter, which is basically a negative mode of the AO. Thus it is rather the preconditioning autumn pressure leading to both the November sea ice anomaly and the AO.

The negative mode of the AO reduces the westerlies in the North Atlantic due to geostrophic winds, and leads to an anomalously cold North European winter. It induces anomalous south-easterly oceanic wind to the Labrador sea, leading to warm conditions there, and northerlies in the Barents Sea, leading to cold conditions. This can also explain the winter sea ice cover (IVa).

The winter response of the different field variables on August and September sea ice anomalies (Fig. 16(Ib) & (IIb)) are quite alike each other and different to the one from November.
This leads to the conclusion that regressions based on August or September sea ice give indications of whether late summer sea ice affects the winter weather, while regressions based on November sea ice rather present the AO and its influence on the winter weather. Regressions on October sea ice describe a state in between and are therefore considered to be of less interest.
Continuing the study, regressions will be based on September sea ice area. Since the August and September sea ice area anomalies show quite similar responses, August could also have been used. To receive seasonal weather predictions, an even longer view to the future could be drawn from August, but the possibly higher robustness of the September SIC signals were favored in this case. The quadratically de-trended September Arctic sea ice area time series will be referred to as ARC.

4.4 Analysis of the Arctic sea ice variability

Kug et al. [2015] observe two winter temperature warm-cold patterns between Arctic and continental mid-latitudinal regions. Warm winter temperatures (DJF) in the Barents-Kara Sea region (30° - 70° E, 70° - 80° N) are associated with severe winters across East Asia, whereas warm winter temperatures in the East Siberian-Chukchi Sea region (160° E - 160° W, 65 ° - 80° N) are associated with severe winters over North America. They also found that the correlation of the winter temperature between the two regions was almost zero.
In the supplementary notes, Kug et al. [2015] note that the warming of the Barents-Kara Sea region was preceded by significant sea ice loss over most of the Arctic in October and November. Winter warming in East Siberian-Chukchi Sea was, on the other hand, not notably preceded by sea-ice loss, and thus, other factors must have led to a warming of this region.

Following their path, it seems interesting to study responses from regional sea ice patterns, since the Arctic apparently does not work as a homogeneous unit.
In the present study, this was done by investigating the influence of the September sea ice area anomalies of two Arctic regions independently. Or, more precisely, the quadratically de-trended September sea ice area anomaly time series of the Arctic (ARC, North of 45° N) was split up in two indexes. One was the Beaufort to East Siberian Sea, including the Chukchi Sea (Be-ES, 140° E - 140° W, 65 ° - 85° N), and the other the Barents-Kara Sea (Ba-Ka, 30° - 90° E, 70° - 85° N) quadratically de-trended September sea ice area anomaly.

The following subsection will show that the sea ice area of these two regions is quite independent of each other, and a weighted sum of both describe the Arctic sea ice area anomaly quite well. This will be shown for ERA-interim, CAM4 and CAM5.

Independency of the two sea ice regions

Figure 17 shows the quadratically de-trended September sea ice area anomaly time series of the Arctic Ocean ($A(t)$, ARC index), the Beaufort to East Siberian ($E(t)$, Be-ES index) and the Barents-Kara Sea ($K(t)$, Ba-Ka index), normalized by their standard deviations. Each index is the time series describing the sea ice area anomaly of its region of definition.

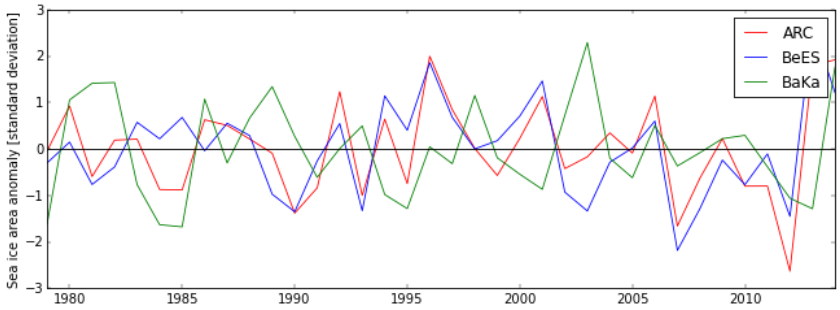

Figure 17: ERA-interim quadratically de-trended September sea ice area of the Arctic Ocean (North of 45° N), the Beaufort to East Siberian Sea (Be-ES, 140° E - 140° W, 65 ° - 85° N) and the Barents-Kara Sea (30° - 90° E, 70° - 85° N) of the years 1979 - 2014. The areas are normalized by their standard deviations.

The correlations of the ARC and Be-ES indexes (c_{AE}= 0.78), and between the ARC and Ba-Ka indexes (c_{AK}= 0.35), are highly significant. This is because the overall sea ice anomaly can be described by the sum of the anomalies its regions.
On the other hand, it is surprising that these two time series are almost uncorrelated, even slightly negatively correlated ($c_{EK} = -0.07$) to each other. One would expect that in a warm Arctic summer, both areas have anomalously little sea ice, and that a cool Arctic summer would yield anomalously much sea ice. But these regions seem to have rather different causes for their summer sea ice retreat. This is interesting, but is beyond the scope of the present study to investigate further. The slightly negative correlation could be caused by winds transporting sea ice from one to the other area, and therefore connect them reversely.

Although $c_{AE} + c_{AK} \approx 1$ and $c_{EK} \approx 0$, the ARC-index $A(t)$ can approximately be described by a weighted sum of the Be-ES-index $E(t)$ and the Ba-Ka-index $B(t)$:

$$A(t) \approx c_{AE} \cdot E(t) + c_{AK} \cdot K(t) \tag{23}$$

Figure 18 shows the September SIC regressed on the September sea ice area anomalies of a) the whole Arctic ($A(x)$, ARC-field), b) the Beaufort to East Siberian Sea region ($E(x)$, Be-ES field) and c) the Barents-Kara Sea region ($K(x)$, Ba-Ka field) from ERA-interim. These are the fields representing one standard deviation of the sea ice area anomaly in its area of definition.

The Be-ES field $E(x)$ and Ba-Ka field $K(x)$ are, in the same way as their time series, quite independent of each other. The Be-ES field show slightly negative anomalies in the Ba-Ka region, and the same is the case for Ba-Ka anomalies in the Be-Es region. This is in line with the slightly negative correlation of the time series. Both patterns show positive anomalies in regions around the defining areas (areas a bit into the Laptev Sea, and the Be-ES around the Queen Elizabeth islands).
A weighted sum of the Be-ES and the Ba-Ka field (Fig. 18(d)) gives a very good approximation of the standard deviation field of ARC (a):

$$A(x) \approx c_{AE} \cdot E(x) + c_{AK} \cdot K(x) \tag{24}$$

This is shown by the difference of the ARC field and the weighted sum in Figure 18(e).
The weighting factors have been derived from the correlation coefficients of the two indexes to the ARC-index (Be-ES: $c_{EA} = 0.78$, Ba-Ka: $c_{AK} = 0.35$).

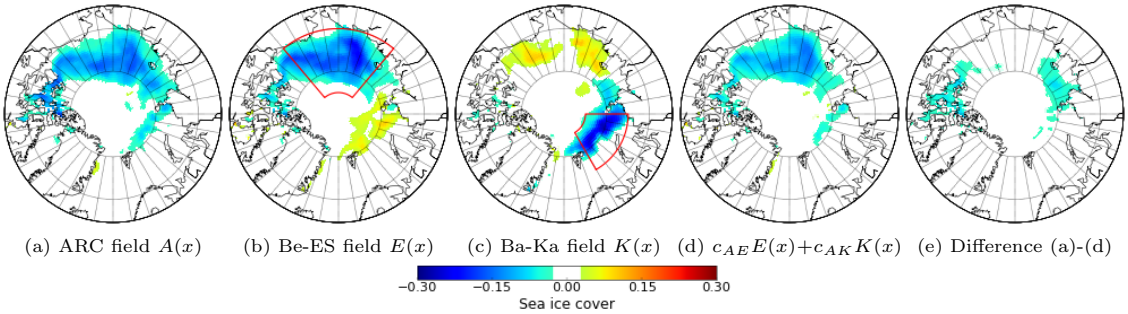

(a) ARC field $A(x)$ (b) Be-ES field $E(x)$ (c) Ba-Ka field $K(x)$ (d) $c_{AE}E(x)+c_{AK}K(x)$ (e) Difference (a)-(d)

Figure 18: ERA-interim September SIC regressed on the September sea ice area anomalies of a) the whole Arctic ($A(x)$, ARC-field), b) the Beaufort to East Siberian Sea region ($E(x)$, Be-ES field) and c) the Barents-Kara Sea region ($K(x)$, Ba-Ka field). These are the fields describing one standard deviation of sea ice area change in its region of definition. Red boxes in b) & c) denote the Be-ES and the Ba-Ka regions.
d) The weighted sum $c_{AE} \cdot E(x)+c_{AK} \cdot K(x)$. c_{AE}/ c_{AK} are the correlation coefficients between the ARC index and the Be-ES/ Ba-Ka index. e) The difference of a) and d).

This shows that the ARC-field can be described in good approximation as a weighted sum of the Be-ES and the Ba-Ka-field.

In CAM4 and CAM5, the procedure yielded the following results:

For CAM4, the ARC-index and Be-ES-index, $c_{AE} = 0.57$ and ARC-index and Ba-Ka-index, $c_{AK} = 0.49$ are highly significantly correlated. The time series of ES-Be and Ba-Ka-index are negatively correlated by -0.23, with a p-value of 0.044, which is just on the border of being significant.
Figure 19 shows the CAM4 September a) ARC ($A(x)$), b) Be-ES ($E(x)$) and c) Ba-Ka ($K(x)$) SIC-fields, representing one standard deviation of the sea ice area anomaly in its area of definition.

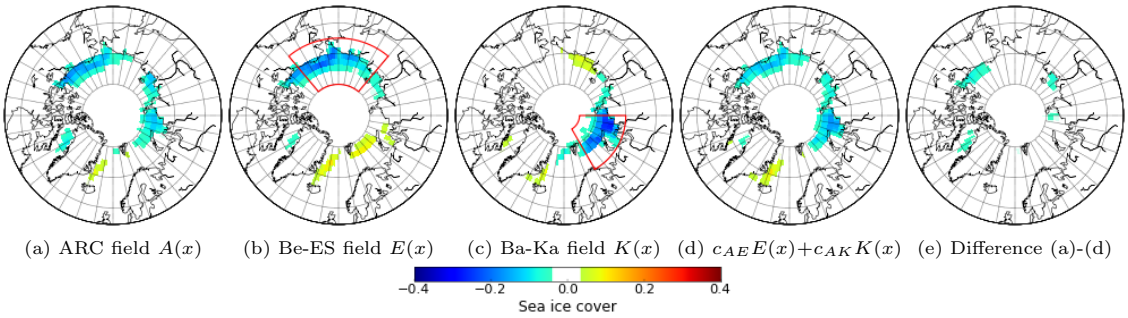

(a) ARC field $A(x)$ (b) Be-ES field $E(x)$ (c) Ba-Ka field $K(x)$ (d) $c_{AE}E(x)+c_{AK}K(x)$ (e) Difference (a)-(d)

Figure 19: As Figure 18, but for CAM4.

The negative correlations between the time series are also evident in the standard deviation fields. The Be-ES field, representing the sea ice reduction of this area, shows small anomalies of increased sea ice in the Ba-Ka field, and the other way round. As for ERA, the SIC anomalies are spread out over the definition areas. A weighted sum of the two fields (Fig. 19(d)) gives a good approximation of the standard deviation field of ARC, which can be seen in the difference between them in Fig. 19(e). The weighting factors were, as for ERA, derived from the correlation coefficients to the ARC-index (Be-ES: $c_{AE} = 0.57$, Ba-Ka: $c_{AK} = 0.49$).

For CAM5, the sea ice area anomaly time series of ARC and ES-Be, $c_{AE} = 0.60$, and ARC and Ba-Ka, $c_{AK} = 0.55$, are again highly significantly correlated. The time series of ES-Be and Ba-Ka are insignificantly negatively correlated with a coefficient of -0.14. The same SIC-fields, representing one standard deviation of the sea ice area anomaly, are shown in Figure 19. They tell the same story as with CAM4.

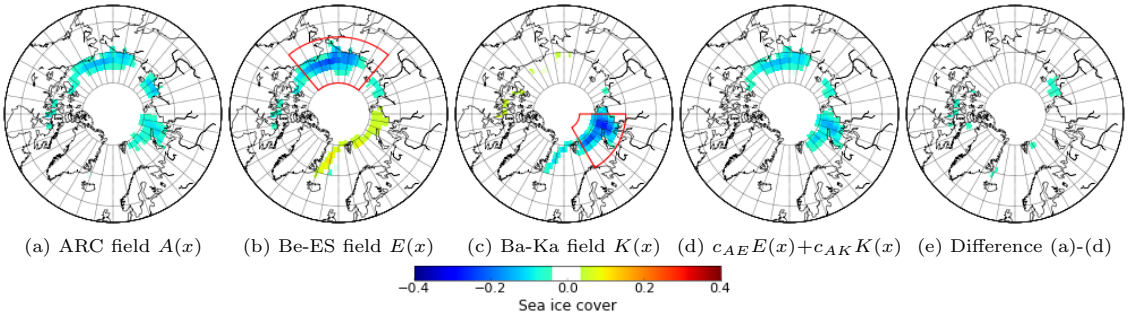

(a) ARC field $A(x)$ (b) Be-ES field $E(x)$ (c) Ba-Ka field $K(x)$ (d) $c_{AE}E(x)+c_{AK}K(x)$ (e) Difference (a)-(d)

Figure 20: As Figure 18, but for CAM5.

The ARC, Be-ES and Ba-Ka SIC fields of CAM4 and CAM5 are quite alike. Their fields do, however, not extend as far north as the ones of ERA. The reason for this is that CAM4 and CAM5 run under pre-industrial and ERA under present day conditions. The climate under pre-industrial conditions was in global average and especially for the Arctic, due to Arctic Amplification, colder than under present day conditions. Therefore the sea ice cover extended further south in the past.
For ERA-interim the contribution of the Be-ES region to the total Arctic sea ice anomalies is much bigger than by the Ba-Ka region, although the Be-ES index has a higher correlation to the ARC index, than the Ba-Ka index. In CAM4 & 5 the Be-ES and the Ba-Ka field have about the same importance in the ARC field.
This knowledge becomes important, when the climatological responses of the Arctic sea ice reduction are explained by a weighted sum of responses to sea ice reduction in the two regions in Chapter 5.4.

This evaluation showed was that the Arctic sea ice variability can be described pretty well by the variability of the Be-ES and the Ba-Ka region. This is working because the sea ice of the two areas is quite independent from each other. The phenomenon was evident in all three models and thus suggests that assuming the Arctic as one unit might be over-simplifying, while analyzing the regions independently and then summing up the results in the end could give more accurate results. The further analysis will use this obtained knowledge and study the effect of the two regions separately.
A devision of responses from sea ice anomalies from the Ba-Ka and the Be-ES region was applied to the ERA-interim, CAM4 and CAM5 data.

5 Effect of Arctic sea ice reduction

In this section, the influence of the late summer Arctic sea ice on the weather in the following autumn and winter season is analyzed.
As mentioned above, the quadratically de-trended September sea ice area index of the whole Arctic (ARC), the Beaufort to East Siberian Sea region (Be-ES, 140° E - 140° W, 65 ° - 85° N) and the Barents-Kara Sea region (Ba-Ka, 30° - 90° E, 70° - 85° N) were obtained for ERA-interim, which presents real climate. The same was done for CAM4 and CAM5, the two model runs with preindustrial conditions, although CAM4 and CAM5 data were Bandpass filtered by periods of more than 4 years instead of quadratically de-trended.
In the first subsection, the responses of different climatological variables of ERA-interim, CAM4 and CAM5 to the Ba-Ka sea ice reduction are compared. In the second subsection, the same is done for the Be-ES sea ice reduction. The third subsection combines the result of the two regional responses and analyzes the influences of sea ice reduction in the whole Arctic.
In the last part, the different scenarios with forced sea ice reduction are used to distinguish the consequences of summer sea ice reduction from common, unknown, underlying causes and natural variability.

5.1 Disappear scenario

The disappear scenario allows one to physically describe the responses of mid-latitude weather to reduced sea ice.
The differences in field variables of the summer 2012 scenario (s12S) and the control run (CR) were calculated as described in the end of Chapter 3.3. They are the differences between the scenario means and the control-run means.

In comparison to the CR, the SIC in the disappear scenario (DS) was reduced radically in summer and autumn. This meant complete disappearance of sea ice in September, while the sea ice cover was less affected in winter and had the same sea ice cover as the control run in February. The fraction of the sea ice area to the maximum area in February for the CR and DS can be seen in Figure 8(a). The December surface energy budget, surface level pressure and surface air temperature differences between the DS and the CR are shown in Figure 21.

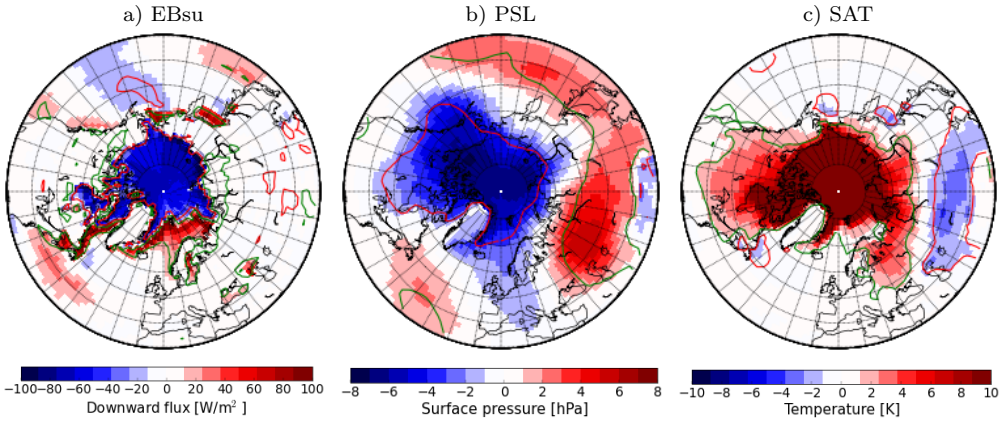

Figure 21: Differences between the CESM disappear scenario and the control run of the December a) surface energy budget (EBsu), the surface pressure (PSL) and the surface air temperature (SAT).

The open water releases energy of up to $150\,W/m^2$ in the reduced sea ice areas (in Oct- Jan). This is mainly because of additional latent heat flux from the ice free oceans, since open water induces more evaporation than sea ice does. In the DS, the surface water temperature was fixed to the freezing point for ice free water. The temperature over ice covered oceans evolves with the physics of the model. Thus, the cold Arctic air is constantly heated by the ice free Arctic ocean. This causes additional long wave radiation and sensible heat, which is released by open water (not shown).
Some of the released energy of the Arctic is taken up by the oceanic regions around it that are sea ice free in both the DS and the CR. Here, the air is warmer in the DS than in CR, but the surface water has the same temperature in both runs. That suggests that the water takes up the energy. This feature can be observed in the ERA-interim and the CESM CAM4 & 5 data as well.
The extra energy release caused by the open water increases the surface air temperature by up to 15° C

over the Arctic Ocean (in Oct- Jan). The anomalously warm air expands and rises, leading to an strong surface low pressure over the area of extra energy release. The polar cell is driven by polar high pressure and mid latitudinal low pressure, and it brings cold northerly air to the mid-latitudes.
This anomalous low pressure weakens the polar cell, which leads to anomalously mid-latitudinal high pressure at the other end of the cell. The reduced cold northerly surface flow is responsible for warm temperatures at the northern edges of the continents.
The anomalous mid-latitudinal low pressure spreads around half the globe from Central Eurasia to the Central North Pacific (Fig. 21(b)). Its anti cyclone strengthens the Siberian high pressure and weakens the westerly winds in Central Eurasia. Therefore, it creates significant cold temperature anomalies of up to 6 ° C in December in Central-East Eurasia.

In the two months before the shown December situation (Fig. 21) the weakening of the polar cell is beginning. The maximum anomalies are reached in December. Thereafter, the weakening wears off and the polar cell gains its original strenght.

The 2012 scenario does not give new or more insights than the disappear scenario, and since the physics are the same, it will not be given its own physical explanation.

5.2 Responses to sea ice anomalies in Barents and Kara Sea

In the following section, the influence of the September sea ice cover of the Barents-Kara Sea (Ba-Ka) on the weather in the extra-tropical Northern hemisphere is analyzed. The Ba-Ka index and the related September SIC fields are described in Chapter 4.4.

Before describing the climatological responses, the sea ice evolution through the autumn and winter, starting with the September anomaly, is presented:
In ERA-interim, September sea ice anomalies from the Ba-Ka region retreat southward, but they are present over the whole winter. CAM4 & 5 show the same picture for this region, although the winter SIC anomalies are smaller than in ERA.
In CAM4 & 5, both regional indexes often show SIC anomalies in regions not associated with their region of origin. As mentioned, the indexes are anti-correlated to each other, although only significant for CAM4. This is expressed by the September SIC field of the Be-ES index showing high sea ice anomalies in the Barents Sea and the other way round (see Fig. 19(b,c)). It may be induced by winds transporting sea ice from one to the other region.

Autumn response

Figure 22 shows the late autumn mean (ON) surface energy budget (EBsu), surface pressure (PSL) and surface air temperature (SAT) regressed on the Ba-Ka index for ERA-interim, CAM4 and CAM5.
The anomalously low sea ice cover in October and November in the Ba-Ka region leads to anomalously high energy fluxes from the surface to the atmosphere. The anomalously warm water, which starts freezing, is a large source of energy to the atmosphere for this region (Fig. 22(a)). Regional anomalously high SAT are the result of this anomalous heat flux from the sea to the atmosphere. They are evident in all three data sets.
The anomalous energy input from the Barents-Kara sea leads to expanding and rising air and creates an anomalously low pressure system at its base (Fig. 22(b)). This is significant for ERA and CAM4 (Fig. 22(I&IIb)). CAM5 shows an anomalous low pressure centered over Eastern Europe.
For ERA, a comparison of the surface pressure with the 300 hPa geopotential height (see Fig. 23(a)) shows that the Arctic low pressure in the upper troposphere is centered over th North pole and a week high pressure exists downstream of this, over East Eurasia. This is a weak anomalous baroclinic situation over Eurasia, which suggest a displacement of the polar jet stream. This further suggests that an anomalous Rossby wave, which propagates eastward until Winter, is induced in autumn. This phenomenon will be described later
Further investigation is needed if these suggestion were to be verified, and if an understanding of the mechanism was to be gained. The upper level wind data could be used for verification of the jet displacement.
In ERA and CAM4, the anomalous surface cyclones in the East Arctic cause anomalously south-westery geostrophic winds in Central Eurasia. This in turn leads to anomalously warm temperatures in Siberia.

All three data sets show areas of significant pressure and temperature anomalies without connection to the Ba-Ka sea ice reductions. These may just be caused by natural variability, although with a significance level of 95%, natural variability still has a 5% chance of creating significant features.

Ba-Ka autumn

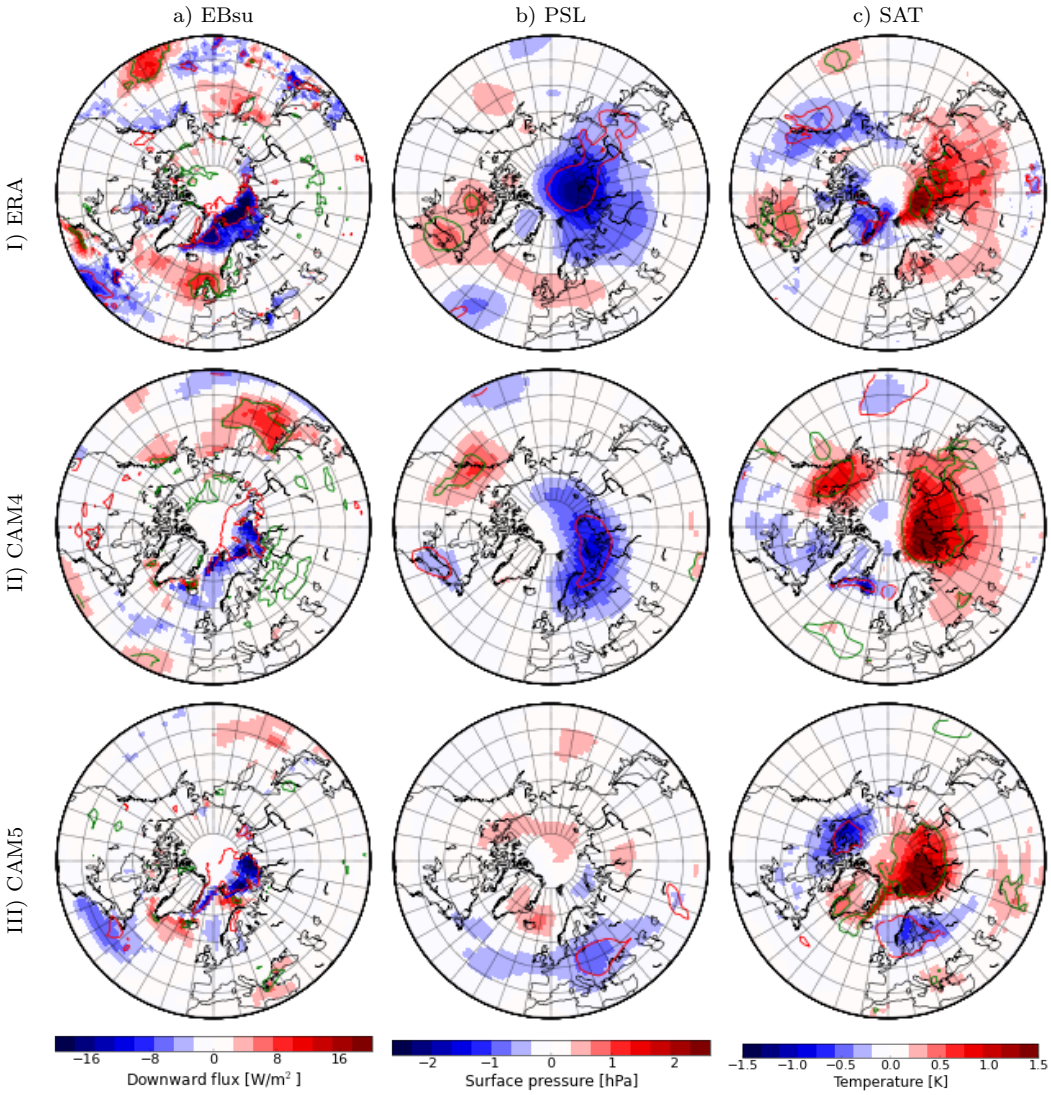

Figure 22: Average autumn (ON) (a) surface energy budget (EBsu), (b) surface level pressure (PSL) and (c) surface air temperature (SAT) lag-regressed on the September sea ice area anomaly of the Barents-Kara Sea (Ba-Ka index). (I) for ERA-interim, (II) for CAM4 and (III) for CAM5. The regression is portrayed negatively to express responses to decreasing sea ice coverage. Red/green contours outline significance at a 95 % level by permutation testing.

Winter responses

Figure 24 shows the winter mean (DJF) surface energy budget (EBsu), surface pressure (PSL) and surface air temperature (SAT) regressed on the Ba-Ka index for ERA-interim, CAM4 and CAM5.

All three data sets show that the Barents and Kara sea still have reduced sea ice in December to February (not shown), leading to anomalously high energy release from the ocean and locally increased temperatures in the Ba-Ka region during the whole winter.
In ERA, the energy release in the Barents-Kara Sea can be made responsible for an anomalously high pressure area over North-Central Eurasia. The explanation for this was given by Honda et al. [2009]. The East Arctic low pressure anomaly and the baroclinic structure in autumn excites a wave train that propagates south-eastward in winter. It forms a surface high pressure over Central Eurasia.

Figure 23(b) shows that the winter atmosphere in the Eastern hemisphere is in a highly baroclinic state. The 300 hPa geopotential height shows a high pressure over the Ba-Ka region and a low pressure over

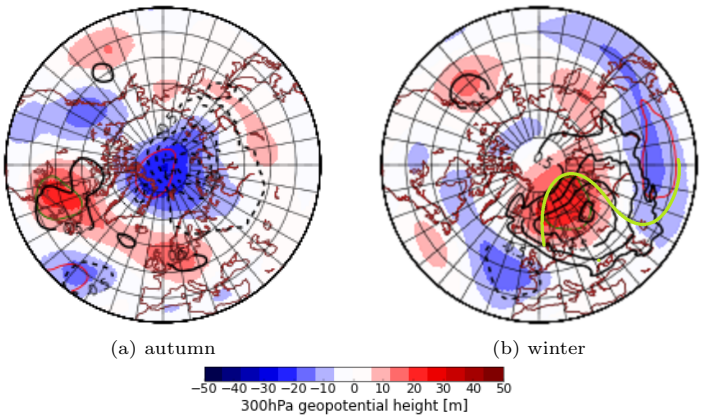

Figure 23: ERA-interim a) autumn (ON) and b) winter (DJF) 300 hPa geopotential height (Z_{300}) regressed on the Ba-Ka index. Regressions are display negatively, to express responses to retreating sea ice. Red/green contours show the 95 % significance level, by permutation testing. Black contours show the corresponding regressed surface pressure field, expressed in Fig. 22(Ib) & 24(Ib) to show barotropic/ baroclinic situations. The green line in b) denotes the anomalous Rossby wave expressed by the pressure state.

South Siberia, while the surface pressure displays a high in Central Eurasia. This can be understood as an anomalous Rossby wave excited by the Ba-Ka heat anomaly.
The Central Eurasian anticyclone is responsible, by geostrophic winds, for anomalously cold northerly and easterly winds from the Arctic and continental regions. These are responsible for cold conditions to Central and East Asia.

The North East Atlantic sees an anomalously high energy uptake for ERA and CAM4, and a heat release for CAM5. The reason is to the atmospheric circulation state. Because of the high heat capacity of the ocean mix layer, atmospheric energy convergence over oceans into an area mostly leads to surface uptake of energy and only small temperature increase. While over land it leads to a warming of the surface temperatures, which has a much smaller heat capacity than the ocean mix layer.

For CAM4, the oceanic energy release in the Ba-Ka region and the energy uptake in the North Atlantic produces a high pressure over Scandinavia. This would be expected to transport cold northerly air to Central Eurasia, but this region observes positive temperature anomalies.
In CAM5 an intensification of the East Arctic low pressure, which was already present in the late autumn (Fig. 22(IIIb)) can be observed. This brings, by strengthening of the westerly flows, anomalously warm air to Northern Eurasia.

From the presented results, it is evident that the winter climate responses in CAM4, CAM5 and ERA are in very high contradiction to each other.

Comparison of the results to [Honda et al., 2009]

Honda et al. [2009] obtain regressed temperature fields for December and February on the linearly detrended sea ice area of a Siberian Coast area (SC, 72-82° N, 30-180° E) using Met Office Hadley Center's sea ice and sea surface temperature data set version 1 (HadISST1) from 1978 - 2006. Thus, the time period is 7 years shorter than the one used in the present study from ERA-interim (1979 - 2014).
The SC responses from Honda et al. [2009] were compared to the responses from the Ba-Ka region. One argument for choosing this region for the comparison is that the Ba-Ka region is included in the SC area. Another is that Honda et al. [2009] made heat flux from the Ba-Ka region responsible for changes in the atmospheric circulation.
The December and February temperature responses from Honda et al. [2009] on the Siberian coast index and from the present study for the Ba-Ka index are shown in Figure 25.
The regressed February temperature fields from Honda et al. [2009] and for the present study both show anomalously cold patterns in Central and East Eurasia. For February temperatures, they are quite alike, but show remarkable differences for December temperatures. For December, Honda et al. [2009] receive strongest responses in East Asia, while the field obtained in this study receives strongest signals in North-

Ba-Ka winter

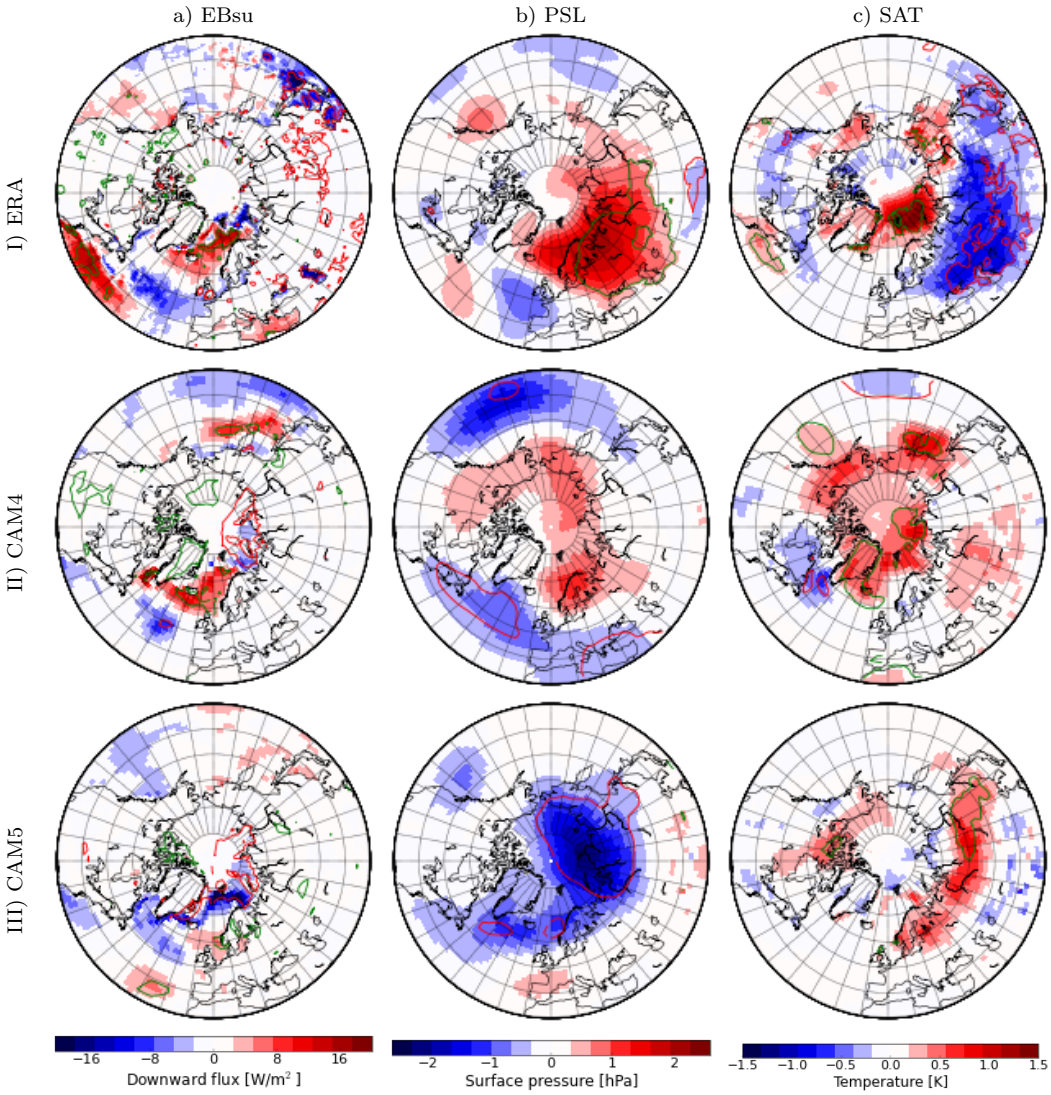

Figure 24: As Figure 22, but for average winter (DJF) fields.

Central Eurasia. The reason lies in the different constructions of the fields, such as differing time series of the data sets, different de-trending of the data, and different sea ice area regions.

The fact that Honda et al. [2009] have comparable results obtained with different methods and data sets gives confidence that September sea ice reduction in the Ba-Ka region favors cold Central Eurasian winter weather. This suggestion is, however, rather opposed by the CAM4 and CAM5 model runs.

Comparison of the results to [Kug et al., 2015]

As mentioned earlier, Kug et al. [2015] observe two winter temperature warm-cold patterns between Arctic and continental mid-latitudinal regions. Warm winter temperatures (DJF) in the Barents-Kara Sea region (30° - 70° E, 70° - 80° N) are associated with severe winters across East Asia, whereas warm winter temperatures in the East Siberian-Chukchi Sea region (Ba-Ka, 160° E - 160° W, 65 ° - 80° N) are associated with severe winters over North America. They also discovered that warm anomalies in the Barents-Kara Sea region were preceded by significant sea ice loss over most of the Arctic in October and November, but they did not conclude on the connection between the summer sea ice area anomaly of the Ba-Ka region to the winter temperatures.

In Figure 26, the correlation between a) the winter temperatures, derived by Kug et al. [2015] and b)

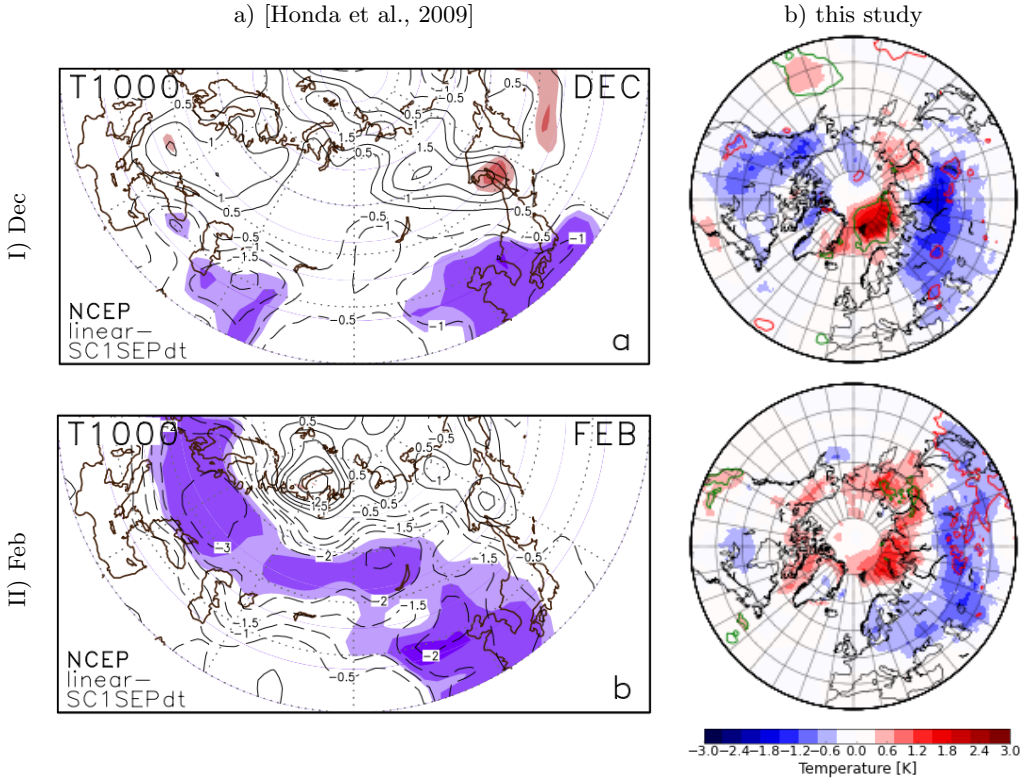

Figure 25: a) From Honda et al. [2009]: HadISST1 monthly mean 1000hPa air temperature of I) December and II) February for 1978/79 - 2005/06 regressed linearly on the September sea ice area of the Siberian coast (SI, 72 - 82° N, 30 - 180° E). Contours correspond to temperature changes when SI decreases by two standard deviations. Areas of shading denote 90, 95 and 99% confidence levels, by Student's t test. b) Same, but ERA interim, from 1979 - 2014 and quadratically detrended. Temperatures are shown for one standard deviation sea ice change in the Barents-Kara Sea. Red/green contours denote a 95% confidence level by permutation testing.

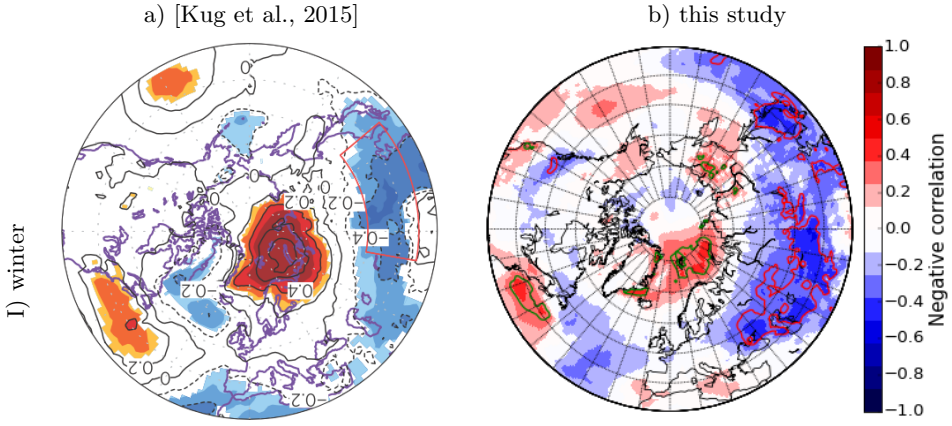

Figure 26: a) From Kug et al. [2015]: Correlation coefficients between the linearly de-trended winter (DJF) SAT anomalies in the Barents-Kara Sea region (ARC1, 30 - 70° E, 70 - 80° N) and the winter SAT anomalies from reanalysis data (1979 - 2014). Shading denotes a significance level of 95 % by Student's t-test. b) Correlation coefficients between quadratically de-trended September sea ice area anomaly in the Ba-Ka region (30° - 90° E, 70° - 85° N)) and winter (DJF) SAT anomalies from ERA-interim data in the same time period. Red/green contours denote a 95% confidence level by permutation testing.

the September sea ice anomaly of the Ba-Ka region to Northern hemispheric temperatures are compared. Both analysis are derived from reanalysis data of the years 1979 - 2014, but different methods of trend correction were chosen. Kug et al. [2015] de-trended the data linearly, while for this study, quadratical de-trending was used. Additionally, the defining area of the Ba-Ka region is slightly different than what was used by Kug et al. [2015].
Apart from these minor difference, the September sea ice anomaly of the Ba-Ka correlates in a very similar way with Northern hemispheric winter temperatures to the way in which the winter Ba-Ka does.
Kug et al. [2015] discovered that the correlation of the Ba-Ka temperatures to the inverse Siberia temperatures is highest with a time lag of 15 days. Still, both are connected by a short time lag, and short persisting atmospheric circulation anomalies could be responsible.
The results obtained by this study show that it is rather the late summer sea ice reduction that is responsible for this warm-cold pattern.
This is a knowledge, which could help to improve long term season weather predictions.

The warm-cold pattern, which Kug et al. [2015] observed between the Be-ES region and North America, is, on the other hand, most likely not a response of September sea ice reduction in the Be-ES region. This will be one result from the next chapter.

5.3 Responses to sea ice anomalies in Beaufort to East Siberian Sea

In this section, focus will be on the responses of the sea ice area anomalies of the Beaufort to East Siberian Sea region (Be-ES). Firstly, the evolution of the sea ice, starting with the September anomalies, is presented.
For ERA-interim, September SIC anomalies in the Beaufort to East Siberian Sea region are still present in October and disappear gradually, ending in December. In CAM4 & 5, the September SIC anomalies decrease in October, are in November mainly present in the Chukchi Sea, and during the rest of the winter, small anomalies occur in the Bering Sea.
For all three data sets, the sea ice cover does not show SIC anomalies in the Be-ES region during the winter, although the surface energy budget anomalies show thinned sea ice, because of higher surface energy release.

Autumn response

Figure 27 shows the late autumn mean (ON) surface energy budget (EBsu), surface pressure (PSL) and surface air temperature (SAT) regressed on the Be-ES index for ERA-interim, CAM4 and CAM5.

In the same way as in the Ba-Ka region, areas of reduced sea ice in October and November emit energy to the atmosphere in the Be-ES region (Fig. 27(a)). This is most prominent in the Beaufort and Chukchi Sea for CAM4 & 5. In ERA, the area of energy emission is larger than for the CAM4 & 5 model runs, which is related to the larger areas of sea ice reduction, as described earlier. It also includes the East-Siberian Sea. The additional induced energy leads to a warming of these areas in all three data sets.

All three models show an anomalous high pressure over the East Arctic and parts of Northern Eurasia. This is upstream of the energy source. Downstream of the heat source, the three datasets show low pressure anomalies. For ERA and CAM5, these anomalies are over Northern North America, opposing the high pressure in the East Arctic. This is might be understood as a change in Rossby wave number one.
CAM4 shows a strengthening of the Aleutian low and a low pressure west of the British Isles. This is a Rossby wave two pattern.

Figure 28(a) shows that the pressure situation induced by the Be-ES sea ice anomaly is rather barotropic in the autumn mean. This is different to the pressure situation induced by the Ba-Ka sea ice anomaly.
Hence, the Be-ES heat source seems to induce a Rossby wave number one or two. The exact reason of occurrence is unclear, but it is surprisingly consistent throughout the data sets. These features, especially the East Arctic high pressure anomaly, possibly caused by a heat source in the Be-ES area, are of high interest and needs further investigation. One could do sensitivity experiments such as the disappear scenario with reduced sea ice or with an artificial heat source for this specific area.

The set up pressure regime influences the surface temperatures. The most pronounced effect, which is observed in all three data sets, is a cold anomaly in Siberia. This is stronger for CAM4 & 5 than for ERA. It is caused by the East Arctic low pressure, bringing anomalously northerly and easterly winds to that area.

Be-ES autumn

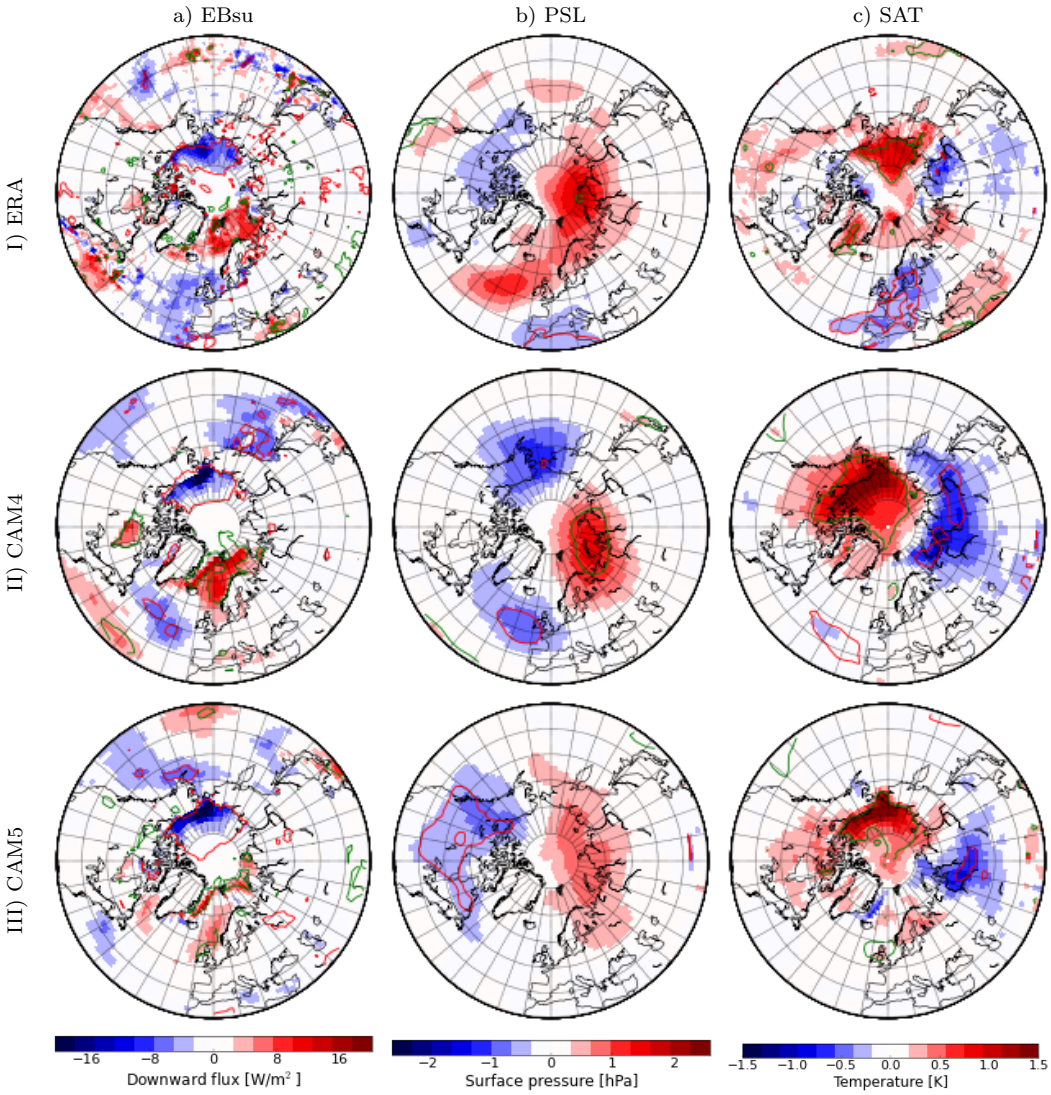

Figure 27: As Figure 22, but for the Beaufort to East Siberian Sea (BeES) index.

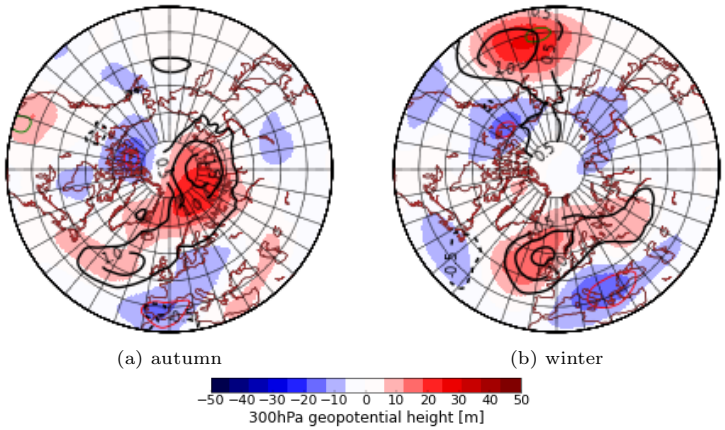

Figure 28: As Figure 23, but for the Beaufort to East Siberian Sea (BeES) index.

Another feature caused by the East Arctic low pressure is high energy uptake in the Barents and Norwegian Seas. The cyclone is responsible for south-westerly winds in that area. The incoming energy is taken up by the ocean mix layer.

Winter response

Figure 29 shows the winter mean (DJF) surface energy budget (EBsu), surface pressure (PSL) and surface air temperature (SAT) regressed on the Be-ES index for ERA-interim, CAM4 and CAM5.

Be-ES winter

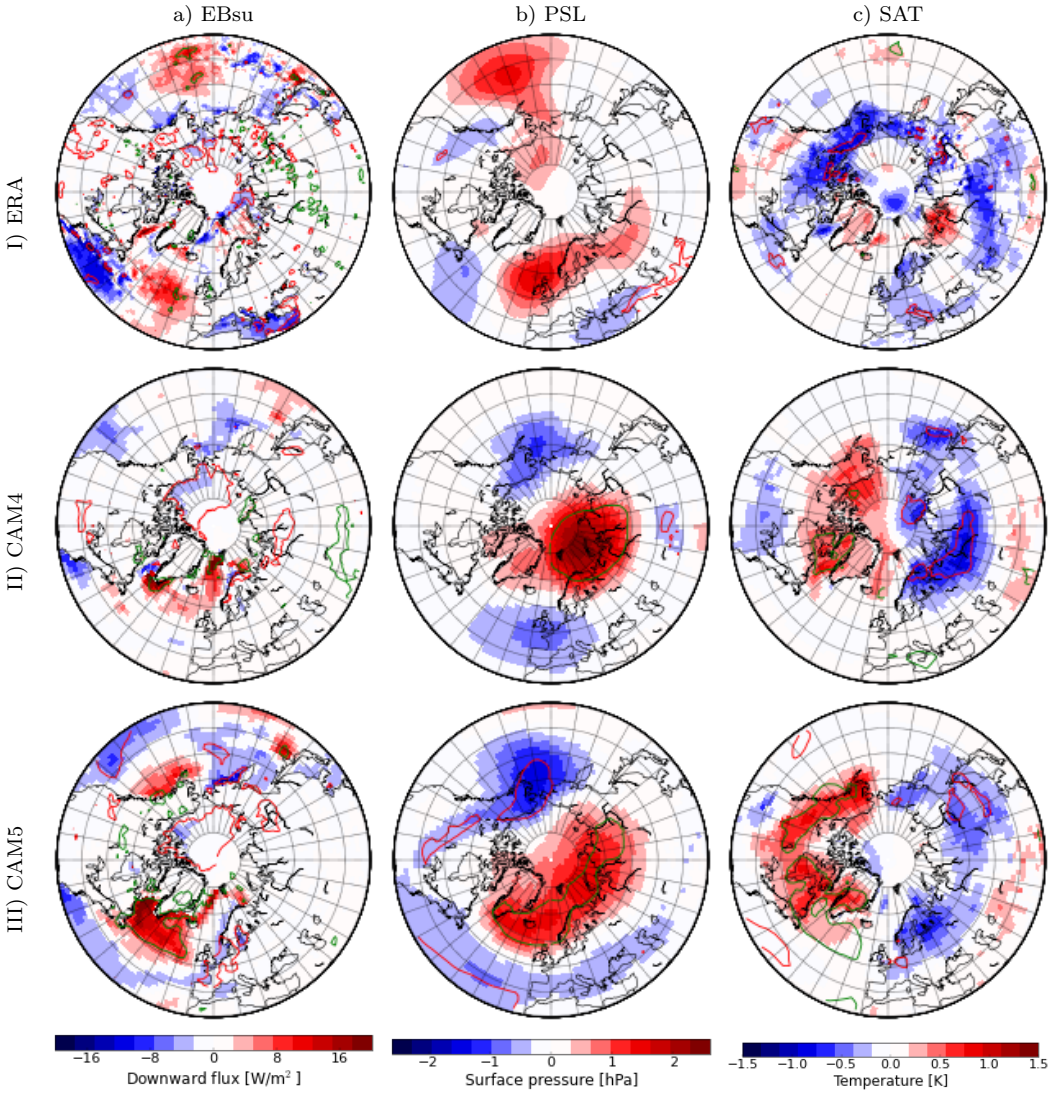

Figure 29: As Figure 22, but for the Beaufort to East Siberian Sea (BeES) index and for average winter (DJF) fields.

The Be-ES region is covered by sea ice in winter. It does, however, see small, but significant heat fluxes from the sea to the atmosphere. These are probably due to thinner sea ice in winter, caused by the sea ice reduction in September. This is valid for all three data sets. They also show more energy release from the Bering Sea, which is in CAM4 & 5 explainable by anomalously little sea ice.
CAM4 & 5 experience a warming of the areas of extra energy release. For ERA, these areas have a slight cooling. This shows that the energy release has only a minor effect.

The Be-ES index for ERA shows an anomalously high pressure between Iceland and the British Islands. This only occurs with high magnitude and significance in February. Reasons for this are unclear. The

anomalous cyclone causes cold conditions in Central Europe by weakening the low pressure systems, bringing warm and wet winter conditions.
The Be-ES index for CAM4 and CAM5 show pressure patterns very alike the negative mode of the Arctic Oscillation (AO), with an intensified high pressure over the East Arctic and low pressures in the mid-latitudinal North Atlantic and an intensified Aleutian low. In CAM4, this pattern is, although less pronounced, already present in the late autumn. CAM5 showed an East Arctic high for late autumn, which amplified in the winter mean.
Both CAM4 and CAM5 show patterns of the AO induced in autumn and relative persistent through the winter. The mechanism for the amplification and persistence of the Arctic high is unclear. A further investigation of this structure would also be interesting.
The temperature is connected in a typical way to the negative mode of the AO: It reduces the westerly flow in Eurasia, leading to cold anomalies in Northern Eurasia. The intensified Aleutian low brings westerly winds to Alaska and North Canada. Intensified high pressures over Greenland and Iceland and low pressures over the Atlantic bring anomalously easterly winds to Newfoundland, leading to warm anomalies there.
Here, ERA and CAM4/5 show very different responses.

To gain a better understanding of the responses to SIC reduction in the two described regions, doing forced model runs with SIC reduction in the two areas separately should be conducted. The September SIC-fields shown in Figure 18 could be used to create scenarios with realistic levels of reduced SIC. If done so, the results could be directly compared to the obtained fields from the Ba-Ka and Be-Es regions shown here.

5.4 Responses to sea ice anomalies in the whole Arctic ocean

Here, the responses to Pan-Arctic September sea ice area anomalies (ARC) are presented. As described in Chapter 4.4 it can be understood as a weighted sum of the two regional indexes. Firstly, the September SIC-fields and the evolution of the SIC in the following autumn and winter are presented for the three data sets.

For ERA-interim, the ARC index SIC field (Fig. 18(a)) shows largest reductions in the Beaufort, Chukchi, East Siberian and Laptev Sea, and between the Queen Elizabeth islands, while the reduction in Barents and Kara Sea are of smaller magnitude. Therefore, the Ba-Ka index has a smaller contribution to the ARC index than the Be-ES index. In October, there is still a strong reduction of sea ice in all the mentioned areas. In November, December and January, reduced sea ice is mainly occurring in the Kara and North Barents Sea.
For CAM4 & 5, both regional indexes contribute with the same amount to the ARC-index.

Autumn response

Figure 30 shows the late autumn mean (ON) surface energy budget (EBsu), surface pressure (PSL) and surface air temperature (SAT) regressed on the ARC index for ERA-interim, CAM4 and CAM5. It also shows the difference of the autumn mean of these variables between the summer 2012 scenario and the control run set up by the CESM.

In the same manner as in the two indexes mentioned before, the ARC index shows that regions with reduced SIC have a net emission of energy to the atmosphere. This leads to increasing temperatures for these regions.
The picture shown by ARC can be made up by a combination of the ones shown by Be-ES and Ba-Ka. The Arctic low pressure induced from the Ba-Ka region, and the Arctic high pressure observed for regressions on the Be-ES index, oppose each other. The low and the high pressures are both significant for ERA and CAM4. For CAM5 they are strong in magnitude, but not significant. The Arctic pressure response to the ARC-index depends on the magnitude of the pressure patterns of the Ba-Ka and the Be-ES index, and the weighting of the two indexes for the ARC-index. The Arctic does not show significant pressure fields for any of the three data sets.
The ARC index for ERA has a North Atlantic high pressure- Central Europe cold temperature pattern, which is significant for the temperatures (Fig. 30(Ib-c)). This is caused by the Be-ES index (Fig. 27(Ib-c)). No connection can, however, be drawn to the Be-ES region, its possible origin, and it is questionable whether this is actually caused by the sea ice anomalies.
Beside the warming patterns for regions of energy release, the regressions on the ARC-index of ERA, CAM4 and CAM5 show only few comparable responses in the autumn mean PSL and SAT. The regional indexes of Be-ES and Ba-Ka show several remarkable responses in line with each other. They do not

ARC autumn

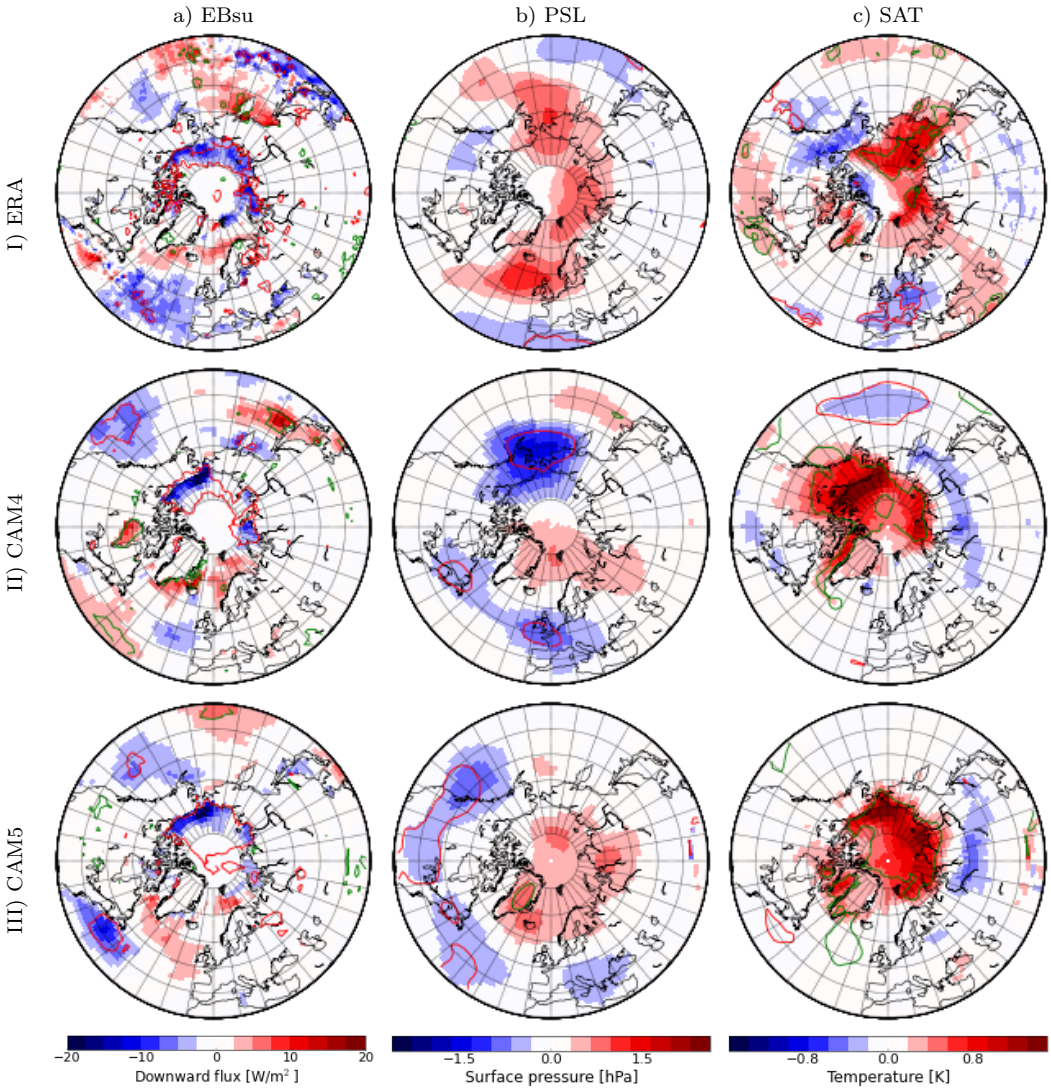

Figure 30: As Figure 22, but for the Arctic (ARC) index.

appear in the ARC index, because the effects of Be-ES and Ba-Ka indexes have different magnitudes and slightly shifted areas of appearance.

This leads to the conclusion that a physical description can rather be given by the two local indexes. The sea ice anomalies of the two regions induce or are connected to different mechanisms, which partly oppose each other.
The effects of the two local indexes therefore mainly cancel out each other, when the responses from Pan-Arctic sea ice anomaly is regarded. Although an evaluation of reduced sea ice in the whole Arctic as one unit does not give clear responses, it is necessary to regard the sea ice reduction of different regions independently.

Winter response

Figure 31 shows the late winter mean (ON) surface energy budget (EBsu), surface pressure (PSL) and surface air temperature (SAT) regressed on the ARC index for ERA-interim, CAM4 and CAM5. It also shows the difference of the winter mean of these variables between the summer 2012 scenario and the control run set up by the CESM.

The ARC index response of the winter mean of the climatological variables can, as for the autumn mean,

ARC winter

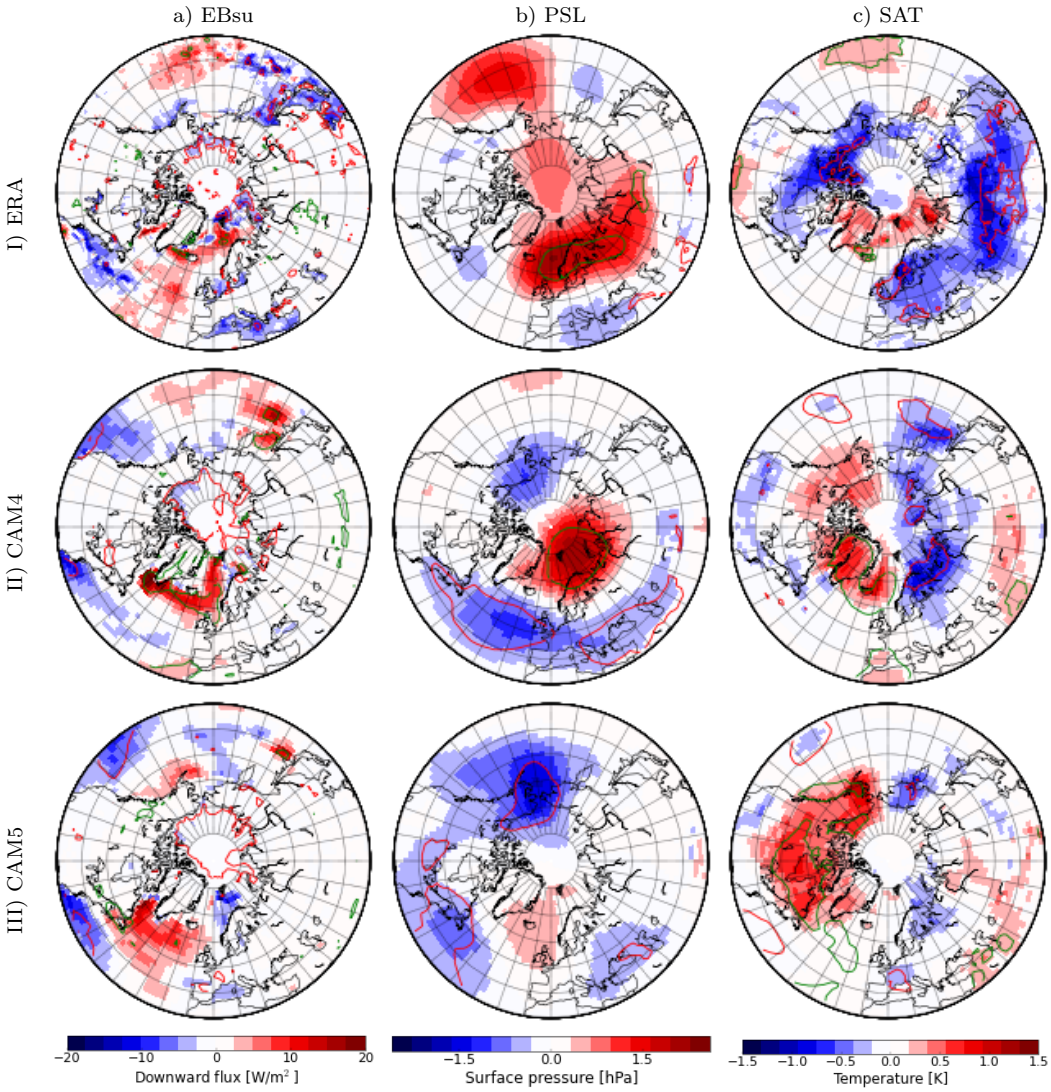

Figure 31: As Figure 22, but for the Arctic (ARC) index and for average winter (DJF) fields.

be understood as a weighted sum of the Be-ES index and the Ba-Ka index response.

For ERA-interim, the warm conditions in the Barents-Kara sea region and the cold conditions in Central and East Asia are from the winter response of the Ba-Ka index (Fig. 24(a)). As explained earlier, an explanation for this could be the induced Rossby wave train, inducing a Central Eurasian high pressure. ERA-interim shows that cold conditions at the North Coast of North America and in Western Europe have their origin in the Be-Es index. There is little evidence supporting their occurrence being due to Be-ES sea ice reduction. Therefore, these patterns are likely caused by natural variability.

CAM4 and CAM5 show Eurasian winter cooling patterns related to Be-ES sea ice reduction and warming patterns for Ba-Ka sea ice reduction. The CAM4 and CAM5 winter response to the Be-ES and the Ba-Ka index also have other remarkable differences from each other and from ERA.

Thus, also the winter response on the ARC-index for CAM4, CAM5 and ERA is in high discrepancy and according patterns are mainly not caused by the same effects, if one goes back to the regional indexes.

5.5 Summer 2012 scenario

In this chapter, the results from the summer 2012 scenario (s12S) are presented. The scenario has forced sea ice conditions similar to the conditions observed for the summer 2012 and is compared to a control run (CR) with climatological SIC forcing. The SIC of the s12S is reduced in relation to the control run (CR) from middle of June to middle of October, as described earlier.
The resulting mean fields of the s12S are compared to the real evolution of the weather in the autumn and winter 2012/13. The difference of the ERA-interim fields of the autumn and winter 2012/13 to the climatological mean will from now be referred to as ERA12.
Both s12S and ERA12 have the same reduced sea ice patterns in summer. These persist for ERA12 and were set to zero for the s12S.

The s12S has a small construction discrepancy, as mentioned earlier. The strongest discrepancy can be seen in the winter surface energy budget in the Hudson Bay (Fig. 33(IIa)). The s12S releases more energy than the CR in December, leading to anomalously high temperatures in that region. Any effects on other regions were not recognized, and no anomalous pressure seems to be induced with origin in that region.

The mean autumn (ON) surface energy budget (EBsu), surface pressure (PSL) and surface air temperature (SAT) of ERA12 and the s12S compared to their climatological mean are shown in Figure 32.

Autumn 2012

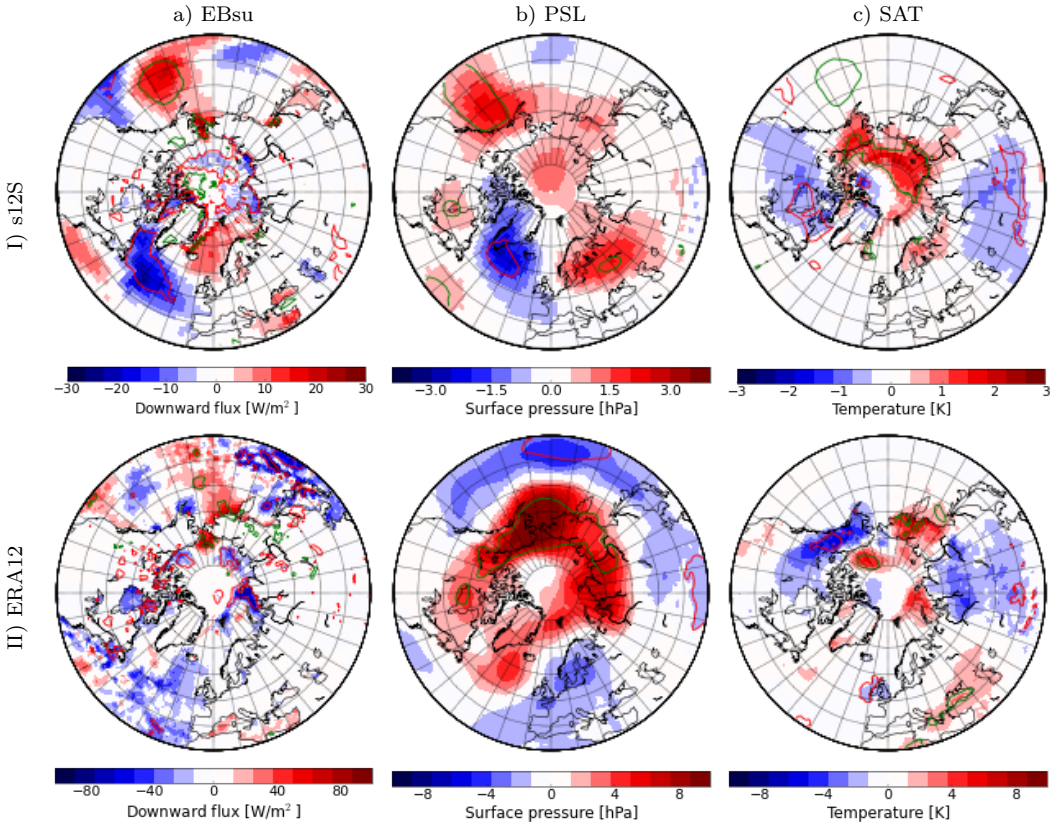

Figure 32: (I) shows the difference of the mean autumn (ON) a) surface energy budget (EBsu), b) surface pressure (PSL) and c) surface air temperature (SAT) between the summer 2012 scenario (s12S) and the control run ensemble mean. (II) shows the difference of the same winter fields of the winter 12/13 and the climatological mean derived from ERA-interim. Red/green contours denote significant values at the 95 % confidence level. Note the different scales.

Both datasets show increased autumn Arctic energy release. This is very strong for ERA12, especially in the Kara Sea.
In s12S, the anomalous energy release is due to the SIC reduction in the first half of October. When the sea ice cover of the s12S is at the state of the CR, there are only minor differences in the surface energy budget.

The sea ice reduction in the late summer and the energy release in autumn leads to anomalously high Arctic temperatures. The autumn surface pressure responses of the two data sets do not show significant features in accordance to each other.

The mean winter (DJF) surface energy budget (EBsu), surface pressure (PSL) and surface air temperature (SAT) of ERA12 and the s12S are shown in Figure 33.

Winter 2012/13

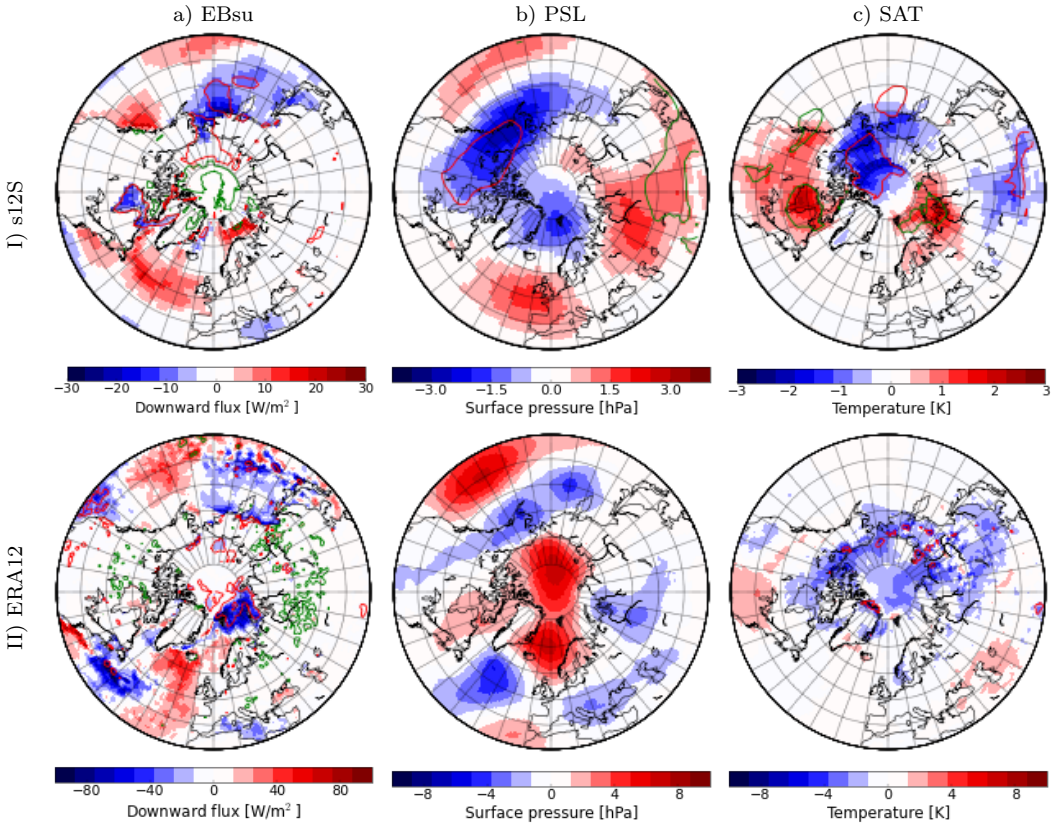

Figure 33: As Figure 32, but for winter (DJF) fields

The s12S shows an anomalous Arctic low pressure also extending over North-west North America. Meanwhile, the East Atlantic and Central Eurasia experience anomalously high pressure.
The temperature anomalies can be described on basis of the pressure situation by geostrophic winds. The intensification of the North-Central Eurasian high pressure is responsible for anomalous easterly cold winds on its south edge, bringing cold conditions to Central Eurasia. It brings anomalous south-westerly winds to the Ba-Ka region leading to warm anomalies there. The low pressure over the West Arctic and North western North America brings anomalous westerly wind to Central Northern America, leading to warm conditions there.
The pressure pattern is of the same kind as the regression of the winter surface pressure on the September Ba-Ka SIC anomaly (Fig. 24(Ib)). To understand its occurrence, further study is needed.
The winter situation for s12S shows both of the winter temperature warm-cold patterns between Arctic and continental mid-latitudinal regions observed by Kug et al. [2015]. One is between the Ba-Ka region and Eurasia and the other between the Be-ES region and North America.
The situation observed in the winter ERA12 by showed a very different winter mean response. It showed large variability between every single month in the fields (not shown), and it is therefore difficult to draw a physical conclusion.

6 Conclusion

To obtain a good analysis of the influence of the late summer sea ice area to the extra-tropical weather, the methods of correlation, regression and composites were compared. Correlations are good to show the strength of a connection, but they do not take into account the magnitude of the response in the units of the fields. This is obtained by regression and composites. The advantage of regression, in comparison to composites, is that they include all the data and they take the magnitude of the sea ice area change into account. Therefore, they are regarded as the more trustworthy tool to obtain the strength of the responding variable.

To analyze effects from the sea ice on other climatological variables, the effect of year-to-year variability of one variable on the year-to-year variability of the other variables was studied. Therefore, as many external effects as possible were excluded. For the ERA-interim data, this was achieved by a quadratical de-trending, since results obtained from linearly de-trending are more vulnerable to underlying external or regional internal effects.
For climate models running with constant atmospheric constitutions, here preindustrial conditions, oceanic modes affect the results. These were diminished by a low-pass filter, excluding modes with an period of more than 4 years. The choice for 4 years was a compromise between excluding the oceanic modes as much as possible, without destroying year-to-year variability.

The sea ice area of the months of September, October and November were tested as base of regression with other variables to investigate how the choice of the month influences the response of the climatological variables in winter. This because one might think that the late summer sea ice anomaly would influence the winter weather mainly due to a connection of late summer and winter sea ice anomalies. Results showed that the significant memory of sea ice in ERA, beside for the Barents-Kara Sea, only lasts until December. Areas that recovered from anomalous low SIC do, however, show anomalously high energy release, probably because of thinned ice. This is significant, but of small magnitude. Pressure and temperature fields have significant and strong responses until the late winter.
The modeling of the summer 2012 scenario, where the sea ice is only changed until the middle of October, show significant responses throughout the winter.
The choice of the sea ice month is of importance for the winter response. Regression on November sea ice area anomalies gives an Arctic Oscillation (AO)-like pattern. It is rather November sea ice anomalies that are caused by the AO than the other way round.
August and September sea ice area anomalies show quite similar responses, and also the August anomalies could have been used, but the possibly higher robustness of the September signals were favored. Correlations do never prove a chain of cause and effect, but the direction of a possible chain is given by the time lagged correlations.

In order to test the observed results, forced model runs were initialized and compared to a Control Run (CR). The forcing was given by a sea ice cover change, while other boundary conditions remained the same in the forced model run and the CR. Therefore, the forcing was responsible for different responses of the model runs.
An extreme scenario with a completely ice free Arctic ocean in September and gradually returning sea ice until full coverage compared to the CR in February was set up and called the disappear scenario (DS). This was used to understand the processes induced by the SIC reduction: The ice free water releases a lot of energy, leading to local warming. The warmed air expands, leading to anomalously low surface pressure. The reduced surface pressure and the reduced poleward temperature gradient weakens the polar cell. Anomalous continental high pressures at the other side of the weakened polar cell could be induced. This high pressure reduce the mid latitudinal westerly flow and bring cold temperature anomalies.
Some of these features can be recognized in ERA, CAM4 & 5.
The, for ERA, quadratically de-trended and, for CAM4 & 5, Bandpass filtered Arctic September sea ice area anomaly is defined as the ARC index.
The ARC index can be split up in the Beaufort-East Siberian Sea region (Be-ES) index and the Barents-Kara Sea (Ba-Ka) index. The latter two indexes are almost independent of each other for ERA-interim and slightly negatively correlated for CAM4 & 5. A weighted sum of the two can describe the sea ice pattern of the ARC index to a fairly high accuracy.

An independent analysis of the sea ice in the two regions revealed that sea ice of the two regions evolves differently throughout the winter, and that the effects are quite different and to some extend opposite to each other.

Negative Arctic sea ice anomalies work as anomalous heat sources, because the warmer ocean water and the refreezing of the ocean releases a lot of energy. Therefore, anomalously high temperatures are observed for these areas for all models and ice indexes.

Negative September sea ice anomalies in the Beaufort-East Siberian Sea region are still present in October, but have vanished in December. For all three models ERA, CAM4 and CAM5, an anomalously high pressure develops in the East Arctic, upstream of the energy source. The physical process is unclear and needs further investigation. The East Arctic anti-cyclone is responsible for cold temperature anomalies in North Siberia.

In CAM4 & 5, this high pressure persists the whole winter in the East Arctic and is responsible for cold anomalies in parts of Eurasia. The persistence of the high pressure was not observed for ERA, and thus, the winter response from the September Be-ES sea ice anomaly is unclear.

Sea ice anomalies in the Barents-Kara Sea (Ba-Ka) persist during the whole autumn and winter, although they retreat southward and weaken. The negative sea ice anomalies in the Ba-Ka region release energy from the ocean to the atmosphere. This warms up the surface air and induces a low pressure over the region. The center and magnitude of the cyclone varies for the three models. The cyclone is responsible for a strengthening of the westerly flow in the mid-latitudes, bringing slightly warmer conditions to Central Eurasia. This autumn cyclone opposes the anti-cyclone observed for the Be-ES index.

Whether the evolution of the weather in winter is induced by Ba-Ka September sea ice anomalies is unclear.
In ERA, an anomalous high pressure is observed in West Russia. It is responsible for anomalous northerly and easterly winds in Central and East Eurasia, leading to significantly colder winter temperatures. This pattern has been described earlier by for example [Honda et al., 2009], but the climate model run of CAM4 does not support it, and the one of CAM5 opposes this winter response to the Ba-Ka September sea ice anomaly.

The autumn and winter responses on the ARC index are very unlike each other. This shows that analyses based on the sea ice retreat of the whole Arctic are problematic. The two described regions have effects, which partly oppose each other. Therefore, the results of analyses based on the whole Arctic sea ice is dependent on the strength of the influence of the two described sea ice regions.

The summer 2012 scenario was set up to test the influence of reduced sea ice only in summer. The obtained autumn and winter fields show very comparable features to the free model runs and observational data, represented by ERA. It showed, to a very high degree, the same responses as the weather in the winter 2012/13.
This gives high support to the hypothesis that the Arctic summer sea ice plays an important role in the evolution of the mid-latitudinal autumn and winter weather.
Whether summer sea ice reduction in the Ba-Ka region leads to cold Central and Eastern Eurasia winters is still questionable. Since the basic state of the atmosphere is changing, responses to sea ice anomalies may differ in the future.

References

Petr Chylek, Chris K Folland, Glen Lesins, Manvendra K Dubey, and Muyin Wang. Arctic air temperature change amplification and the atlantic multidecadal oscillation. *Geophysical Research Letters*, 36(14), 2009.

DP Dee, SM Uppala, AJ Simmons, Paul Berrisford, P Poli, S Kobayashi, U Andrae, MA Balmaseda, G Balsamo, P Bauer, et al. The era-interim reanalysis: Configuration and performance of the data assimilation system. *Quarterly Journal of the Royal Meteorological Society*, 137(656):553–597, 2011.

John T Fasullo and Kevin E Trenberth. The annual cycle of the energy budget. part ii: Meridional structures and poleward transports. *Journal of Climate*, 21(10):2313–2325, 2008.

Jennifer A Francis and Stephen J Vavrus. Evidence linking arctic amplification to extreme weather in mid-latitudes. *Geophysical Research Letters*, 39(6), 2012.

Rune G Graversen, Thorsten Mauritsen, Michael Tjernström, Erland Källén, and Gunilla Svensson. Vertical structure of recent arctic warming. *Nature*, 451(7174):53–56, 2008.

Rune G Graversen, Peter L Langen, and Thorsten Mauritsen. Polar amplification in ccsm4: contributions from the lapse rate and surface albedo feedbacks. *Journal of Climate*, 27(12):4433–4450, 2014.

Meiji Honda, Jun Inoue, and Shozo Yamane. Influence of low arctic sea-ice minima on anomalously cold eurasian winters. *Geophysical Research Letters*, 36(8), 2009.

James W Hurrell, Marika M Holland, Peter R Gent, S Ghan, Jennifer E Kay, PJ Kushner, J-F Lamarque, William G Large, D Lawrence, Keith Lindsay, et al. The community earth system model: a framework for collaborative research. *Bulletin of the American Meteorological Society*, 94(9):1339–1360, 2013.

Jong-Seong Kug, Jee-Hoon Jeong, Yeon-Soo Jang, Baek-Min Kim, Chris K Folland, Seung-Ki Min, and Seok-Woo Son. Two distinct influences of arctic warming on cold winters over north america and east asia. *Nature Geoscience*, 2015.

James A Screen. Influence of arctic sea ice on european summer precipitation. *Environmental Research Letters*, 8(4):044015, 2013.

Mark C Serreze and Roger G Barry. Processes and impacts of arctic amplification: A research synthesis. *Global and Planetary Change*, 77(1):85–96, 2011.

Julienne C Stroeve, James Maslanik, Mark C Serreze, Ignatius Rigor, Walter Meier, and Charles Fowler. Sea ice response to an extreme negative phase of the arctic oscillation during winter 2009/2010. *Geophysical Research Letters*, 38(2), 2011.

Kevin E Trenberth, John T Fasullo, and Jeffrey Kiehl. Earth's global energy budget. *Bulletin of the American Meteorological Society*, 90(3):311–323, 2009.

David G Vaughan, Josefino C Comiso, Ian Allison, Jorge Carrasco, Georg Kaser, Ronald Kwok, Philip Mote, Tavi Murray, Frank Paul, Jiawen Ren, et al. Observations: cryosphere. *Climate change*, pages 317–382, 2013.

Qigang Wu and David M Straus. Ao, cowl, and observed climate trends. *Journal of climate*, 17(11): 2139–2156, 2004.

Xiao-Yi Yang, John C Fyfe, and Gregory M Flato. The role of poleward energy transport in arctic temperature evolution. *Geophysical Research Letters*, 37(14), 2010.

[1]: http://www.ic.ucsc.edu/ wxcheng/envs23/lecture5/13_12global_wind.JPG
[2]: http://www.webpages.uidaho.edu/ simkat/cors220_files/atmospheric_circulation.jpg
[3]: http://www.goes-r.gov/users/comet/tropical/textbook_2nd_edition/navmenu.php_tab_4_page_2.3.0
[4]: http://apollo.lsc.vsc.edu/classes/met130/notes/chapter12/cold_warm_air_advection.html
[5]: http://www.cpc.ncep.noaa.gov/products/precip/CWlink/daily_ao_index/ao.loading.shtml